Quantitative analysis of rabies virus-based synaptic connectivity tracing

Alexandra Tran-Van-Minh[1,#], Zhiwen Ye[1,#] and Ede Rancz[1,2,*]

[1]The Francis Crick Institute, London, UK
[2]INMED, INSERM, Aix-Marseille Université, France
[#]These authors contributed equally.
[*]correspondence to ede.rancz@inserm.fr

Abstract

Monosynaptically restricted rabies viruses have been used for more than a decade for synaptic connectivity tracing. However, the verisimilitude of quantitative conclusions drawn from these experiments is largely unknown. The primary reason is the simple metrics commonly used, which generally disregard the effect of starter cell numbers. Here we present an experimental dataset with a broad range of starter cell numbers and explore their relationship with the number of input cells across the brain using descriptive statistics and modelling. We show that starter cell numbers strongly affect input fraction and convergence index measures, making quantitative comparisons unreliable. Furthermore, we suggest a principled way to analyse rabies derived connectivity data by taking advantage of the starter vs input cell relationship that we describe and validate across independent datasets.

1 Introduction

Understanding synaptic connectivity is important to unravel the workings of the nervous system. Recently developed variants of modified rabies virus provide a powerful tool to determine the upstream connectivity of neuronal populations or even single neurons [1–4] at the level of the whole brain, a feat currently unattainable by other means. Monosynaptically restricted connectivity tracing [5,6] can be initiated in neuronal populations defined in various ways, for example genetically [7], functionally [8] or by projection targets [9]. This method offers a highly quantifiable measure with single-cell resolution, i.e. individual rabies infected neurons. When combined with whole-brain imaging and segmentation, this approach can reveal high-fidelity input connectivity maps. It is hard however to precisely control the number of starter cells labelled by initial virus injection. This source of variability is usually ignored, as it is often assumed that the brain-wide number of input cells (n_i) scales linearly with increasing number of labelled starter cells (n_s) [10–15]. Although it is a reasonable assumption that n_i increases monotonically with n_s, a linear relationship between n_i and n_s would require that labelled starter cells do not share any presynaptic input cell, and that the pool of input cells is infinite. These assumptions are biologically implausible, and the exact relationship between n_i and n_s remains largely unexplored. This is in part because most rabies tracing studies are performed on small numbers of brains, starter cells are not quantified, or input cells may have been counted only in selected parts of the brain. Indeed, the advent of automated pipelines for registration and cell counting in whole-brain images is relatively recent [14, 16, 17], and without these pipelines, whole-brain cell counting for large datasets was an extremely time- and labour-intensive process. In addition, various methods are used to analyze rabies tracing experiments. Metrics used in previous studies include input fraction (the inputs count per area relative to either the total number of input cells in the brain, sometimes referred to as total input fraction, [15, 18–21], or relative to the number of input cells in a given area [15, 22] or layer [23]), and the convergence index, also called input connection strength index or input magnitude (area inputs count normalized by number of starter cells [18,20,24–26]). The disparity in methods and terminology used to report the properties of connectivity maps complicates direct comparisons across various studies.

Here we set out to explore the relationship between the number of starter and input cells. We generated a comparatively large dataset with a broad range of starter cell numbers in layer 5 of mouse visual cortex. We then used descriptive statistics, model selection and numerical modelling of connectivity to explore the data, and compare various analysis approaches. We find that the relationship between number of the starter cells and number of the labelled input cells is non-linear, and that the range of starter cells differently affects some of the metrics commonly used to analyze connectivity maps. Using these results we suggest principles for experiment design and appropriate analysis methodologies to use depending on the data available and on the desired information to be extracted.

2 Results

We carried out rabies tracing experiments initiated in layer 5 pyramidal neurons (L5PN) in mouse primary and secondary visual cortex. We followed previously described protocols [3] using the G-protein deleted, EnvA pseudotyped version of CVS-N2c rabies

virus [6]. To achieve a wide range of starter cell numbers, we used different labeling strategies. We took advantage of varied cell densities in Cre driver lines labeling L5PNs, or through retrogradely labeling L5PNs by injecting retrograde AAV viruses to their projection targets. In addition, we also varied the volume of the injected helper viruses. Our dataset is thus uniform in terms of cell-type (L5PN), yet contains sufficient heterogeneity in terms of sub-types and starter areas to test comparative approaches. Whole brains were imaged using 2-photon tomography, then registered, segmented and annotated according to the Allen Common Coordinate Framework (CCFv3, [27]) using the open source brainreg software [17]. Starter and input cells were detected and classified using the open source software cellfinder [28]. Area-wise cell counts for individual experiments are reported in Suppl. Data File 1.

We use the following nomenclature throughout. Starter cells (also called postsynaptic, host or target cells in the literature) are neurons for which rabies tracing was initiated, and their count is denoted by n_s. Neurons labelled after the transsynaptic jump, and thus considered first-order presynaptic to starter cells, are called input cells and their count in the entire brain is denoted by n_i. Starter and input areas are brain areas defined according to the CCFv3 containing starter or input cells, respectively. Brain area names and abbreviations are from the Allen Common Coordinate Framework (CCFv3, [27]).

2.1 The relationship between input and starter cells is non-linear and is best described in log scale

We took advantage of the broad range of starter cell numbers and the large number of experiments in our dataset to investigate the nature of the n_i vs n_s relationship. First, we fitted whole-brain n_i vs n_s data with linear, quadratic, exponential and power-law functions as well as a growth model that describes the labeling of input cells at a given rate, and considering a maximum number of input cells that can be labeled (Fig 1A). We then performed model selection using the Akaike Information Criterion corrected for small sample sizes (AIC_c) [29]. From the model selection procedure, the power-law model and growth models are the best candidates (Table 1). However, residuals showed strong heteroscedasticity when standardized residuals were plotted against the fitted values (Fig 1B). In such cases, logarithmic transformation may allow to adjust the data distribution to a less skewed, more Gaussian-like distribution [30]. Model selection was next performed on log-transformed data and gave support for the fitting of a linear model, as the addition of a quadratic term did not improve the model fit (Fig 1C, Table 2). The plots of standardized residuals vs fitted values suggest a better normality of residuals in the case of log-transformed data (Fig 1B, D). There are thus two possible error models: log-normal distributed errors based on untransformed data, or normally distributed errors based on fitting log-transformed data. We tested these possibilities by fitting two models in which the likelihood form explicitly includes the error structures [31]. The two resulting models were then compared using the AIC_c and confirmed support for the log-normal error model (Table 3). Consequently, we used log-transformed n_i and n_s data for further analysis.

To test the generality of our conclusions, we performed model selection and error model analysis on datasets from published studies performed on a range of cell types and starter brain areas, using different imaging and cell counting approaches as well as employing various rabies virus strains and G-proteins [13–15, 18, 19, 22, 25, 32–36]. The analysis revealed statistical support for the power-law and growth models for untransformed n_i vs n_s data, a linear model for the log-transformed data, and for the log-normal

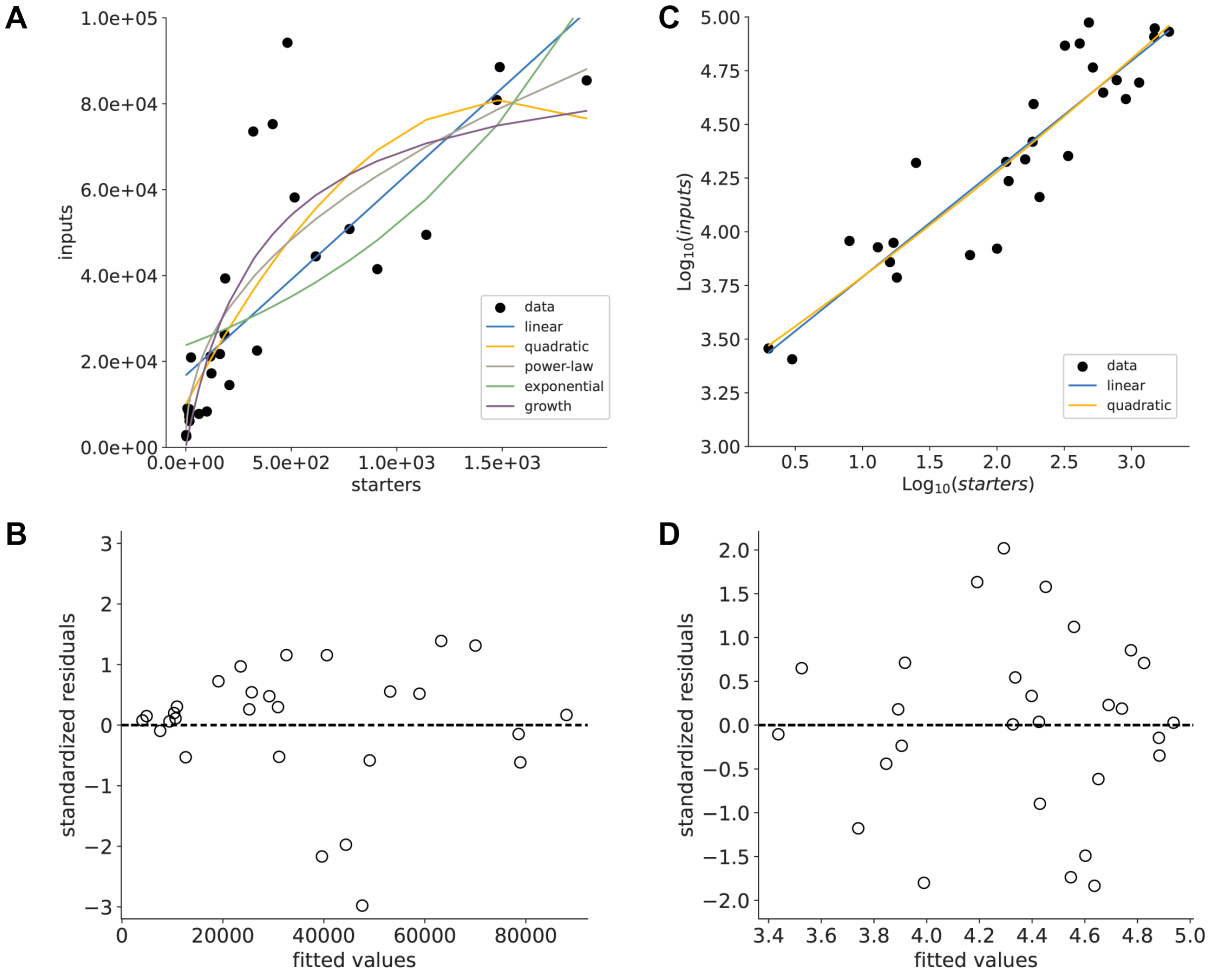

Figure 1: **Model comparison for whole-brain data** (A) Number of input cells vs starter cells. Colours indicate different fitted models (blue - linear; yellow - quadratic; grey - power law; green - exponential; purple - growth). (B) Distribution of standardized residuals for the power-law fit. (C) Same as in A, but on log-transformed data. (D) Same as in B, but for the linear fit on log-transformed data.

error model (Fig S1, Tables 1, 2, 3) across most datasets. Therefore, the growth of labelled inputs with the number of starter cells follows broadly the same statistical rules independently of experimental conditions and is not specific to our dataset. Furthermore, this generality allowed us to investigate whether rabies strains may affect the parameters of the n_i vs n_s relationship. We used a linear classifier to determine whether the rabies strain used could be identified using the $\log(n_s)$, $\log(n_i)$ and the broad class of starter cells (pyramidal or interneuron) as features. The classifier could predict the rabies strain with 82% accuracy (Fig S2) and revealed a general trend where brains labelled using the CVS-N2c rabies strains displayed higher input cell counts for a similar number of starter cells, consistent with a higher trans-synaptic yield of the CVS-N2c strain [6].

We next built a probabilistic connectivity model (Fig S3) and explored the influence of various model parameters on the structure of the data. This model assumes that for a given input area I containing N_I cells, each input neuron connects with a given starter neuron with probability p. This model allows us to simulate a rabies tracing experiment, by selecting a number n_s of starter neurons, and building a simulated connectome of all their connections with area I. From each modeled connectome, we can then calculate n_i, the total number of unique neurons in I connected to the n_s starter neurons. In

order to represent variability across brains, the model parameters (connection probability p and input pool size N_i) were sampled from Gaussian distributions for each simulated connectome (Fig S4A). The resulting n_i vs n_s curve displays a strong skewness of residuals, similar to the experimental data (Fig S4B). This process was repeated 100 times with random sampling, and we performed the error model analysis for each resulting n_i vs n_s curve. The distribution of resulting AIC_c values shows a consistent, strong support for the log-normal error model (Fig S4C). Therefore, the probabilistic model, built with minimal assumptions and small number of parameters, is sufficient to generate n_i vs n_s relationships with a log-normal error distribution, similar to that of the experimental data.

2.2 Input vs. starter relationships parameters differ across input areas

For further analysis, we have selected 19 functionally diverse input areas (Table 4). To determine whether the number of input cells from individual brain areas displayed similar form and error structure as the whole-brain data, we applied the same model selection procedure and error model analysis to a selection of functionally diverse input areas (Table 4). The $AICc$ analysis showed that the n_i vs n_s relationship is better fitted by the power-law and growth models using the untransformed data for all areas (Table 4), and by a linear model using the log-transformed data (Table 5). In addition, the error model analysis supported a log-normal distribution of residuals (Table 6). We thus fitted the log-transformed n_i vs n_s relationship per input area with a linear model and observed that the resulting fit parameters, y-intercept and slope were correlated and covered a broad range of values (Fig 2A, Fig S5).

Next we performed simulations using the probabilistic model to try to capture the diversity of input areas by varying systematically the model parameters across a large range. Results from these simulations were log-transformed and fitted with a linear model. The slope vs y-intercept relationship showed similar interaction and range to our data-set (Fig 2B). Furthermore, larger values of N_i produced on average higher y-intercept values, while higher values of p were associated with lower slope values (Fig S6). Varying the width of the input parameter distributions did not affect the mean slope and y-intercept values (Fig S7).

The connectomes generated by the probabilistic model are unidirectional bipartite networks and can be analyzed for their network properties, such as their node degree distribution. The in-degree of starter cells (deg_s) corresponds to the number of input cells a single starter cell is contacted by, while the out-degree of input cells (deg_i) corresponds to the number of starter cells a single input cell contacts (Fig S3). We decided to investigate how starter and input cell degrees were affected by model parameters, as n_i and n_s varied broadly. Analysis of the degree distributions of both starter and input pools revealed them to vary with both model parameters to various extents (Fig S8). Next we tried to assess whether manipulating specifically the degree distributions of starter or input cells would affect y-intercept and slope values of the resulting networks. To this end we used a bipartite network configuration model where average degree distributions of both starter and input cells can be declared explicitly (Fig S9). The resulting $\log(n_i)$ vs $\log(n_s)$ relationship were fitted with a linear model as previously. Changing deg_s affected primarily the y-intercept values, which increased with the mean in-degree of the starter pool, but had little effect on the slope. In contrast, varying deg_i affected primarily the slope, with increasing mean out-degree of the input pool corresponding to lower slope values (Fig 3, S 10). This suggests that the intercept of the $Log(n_i)$ vs $Log(n_s)$ is mainly

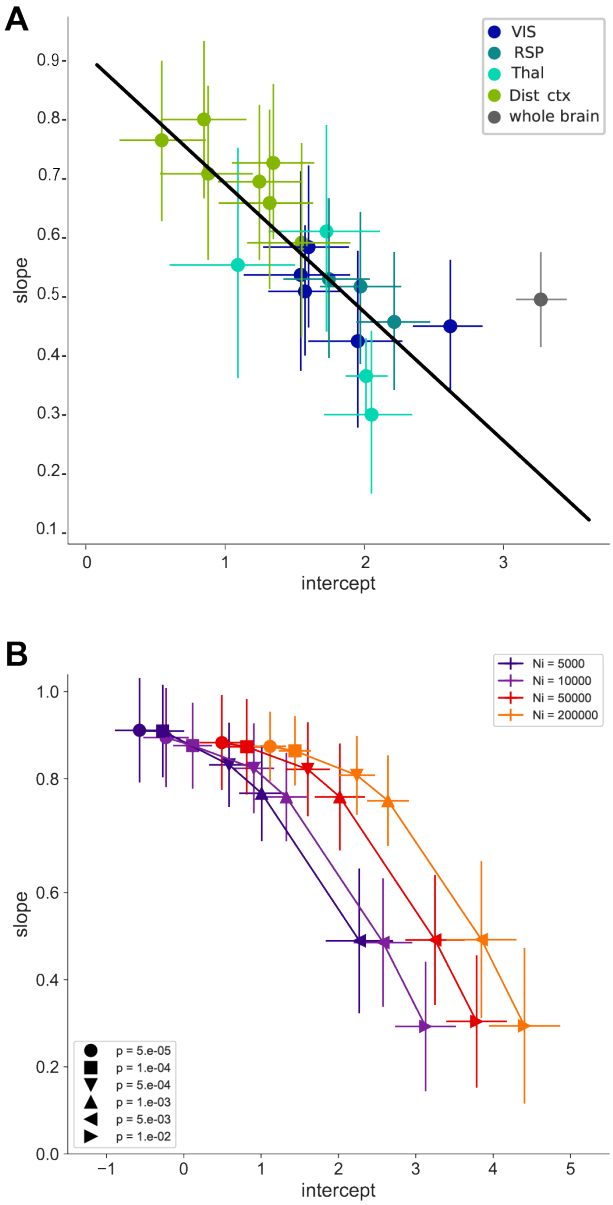

Figure 2: **Distribution of slope and y-intercept values for different input areas** (A) Slope vs y-intercept relationship for individual input areas. Colors indicate functional grouping of brain areas (VIS (dark blue) : VISp, VISpm, VISam, VISl, VISal; RSP (blue): RSPv, RSPd, RSPagl; Thal. (cyan): LP, LD, AM, LGd; Distal cortex (green): ORB, ACA, AUD, PTLp, TEa, MOs, CLA). Whole-brain data is shown in gray. Black line is a linear fit through all data points except the whole-brain data. Error bars are 95% confidence intervals calculated using residuals resampling. (B) Data from simulations using the probabilistic model over a range of parameters (N_i, represented by the different colours, and p, indicated by different markers).

affected by the convergence of presynaptic inputs onto single starter neurons, thus the measured y-intercept translates into the number of input cells to a single starter cell. The slope, on the other hand, is mostly determined by the amount of divergence of input cells with respect to the starter cells.

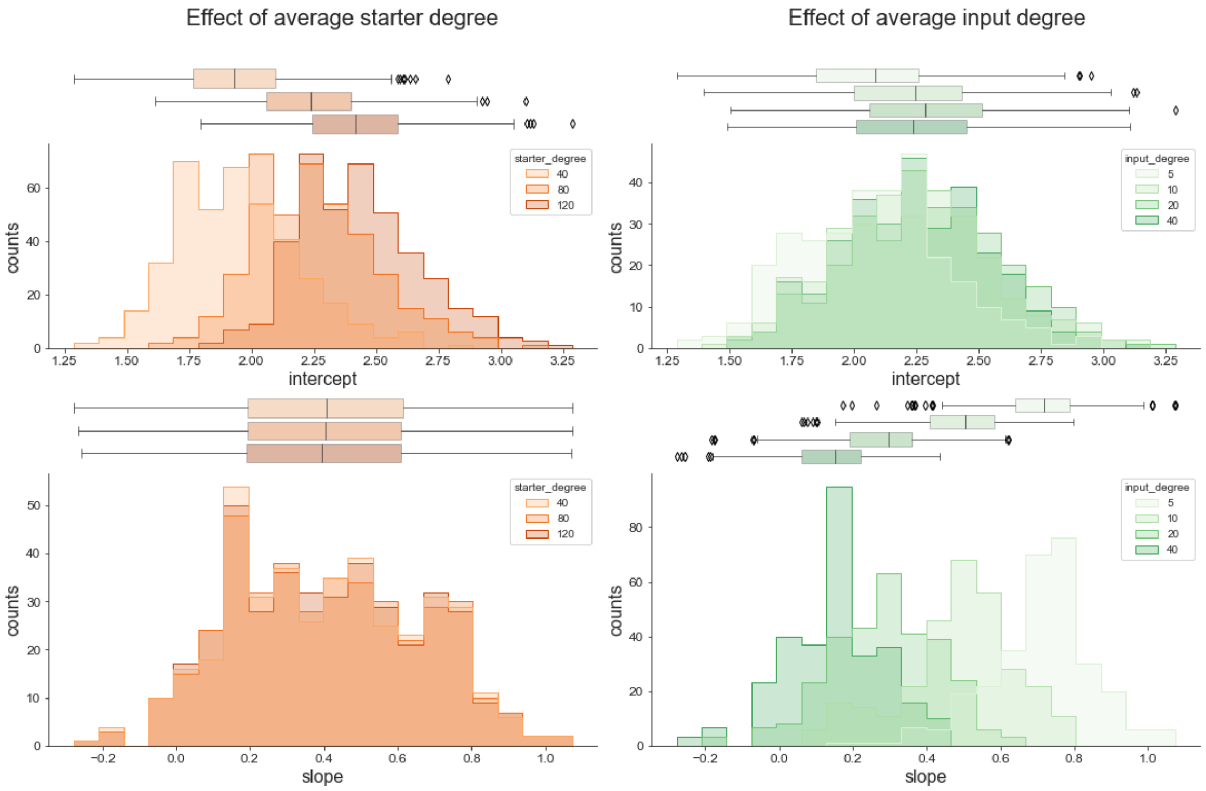

Figure 3: **Effect of degree distribution of input and starter sets on slope and y-intercept values** Average degree distribution of either the starter (orange) or the input (green) pools were specified using a configuration model and varied separately. $\log(n_i)$ vs $\log(n_s)$ relationships of the resulting networks were fit with a linear model to extract y-intercept and slope values.

2.3 Area input fractions depend on the number of starter cells

Area input fraction (often called "input proportion" or "input fraction" in the literature) is a measure commonly used in rabies tracing studies to reveal input patterns and compare them across experimental conditions such as genetic identity or the location of starter cells populations [14, 15, 19, 22, 25]. It is defined as the number of labelled input cells in a given brain area normalized by n_i. This calculation however disregards the range of starter cell numbers and thus implicitly assumes that area input fractions scale with n_s in a uniform fashion across all input areas, an assumption which remains to be tested directly. When n_s is known, another measure called convergence index (also called connectivity ratio or connectivity strength index) is also often reported in the literature. This is calculated by normalising area-wise input cell numbers by n_s and thus it can only provide an n_s independent measure if individual starters cells do not share any of their input cells, a biologically highly unlikely scenario.

Multiple previous studies used multivariate linear regression to evaluate the relative contribution of various experimental parameters on input fraction patterns [15, 19]. We thus used linear regression analysis on area input fractions and included starter cell number as one of the parameters, either as a single predictor or in combination with other regression variables (the genotype or the location of starter cells). We found that the best predictor of area input fraction variations was the starter cell number for many input areas (Fig 4A, S11).

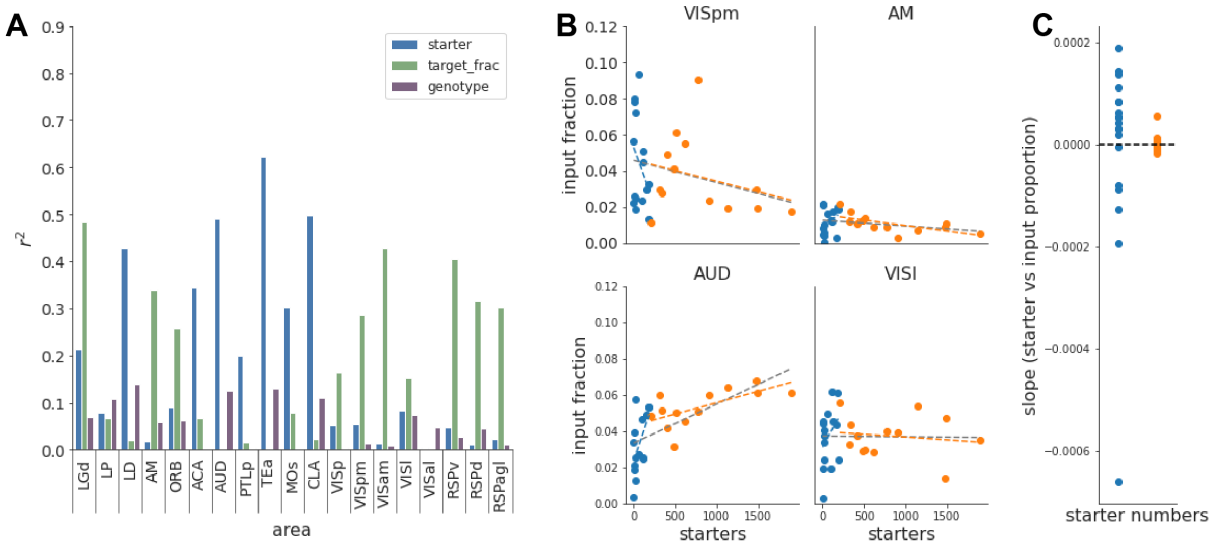

Figure 4: **Effect of starter number on area input fraction** (A) Multivariate linear regression between the area input fraction and starter cell number, location or genotype of starter cells. (B) Area input fraction vs starter relationship for four example areas. Dashed lines are linear fits through the data, for the full dataset (grey line), starters < 200 (blue line) or starters > 200 (orange line) (C) Slope of the area input fraction vs n_s relationship for low (blue) or high starter numbers (orange).

Given the prominence of the number of starter cells as a predictor of area input fractions, we next explored its interaction across the range of starter cells in our dataset. We plotted the area input fraction as a function of starter cell numbers for each input area (Fig 4B, S12A). These plots reveal that area input fractions scale with n_s in a highly diverse fashion across areas, with area input fraction vs n_s relationships being either increasing or decreasing for low n_s values, and become asymptotically horizontal for high n_s values. Furthermore, the area input fraction vs n_s relationships have a wider spread for low n_s values(Fig 4B, C, S12A). Input areas where n_s was a weak predictor of area input fraction in the regression model (e.g. VISl, RSPd, AM) display an accordingly steady area input fraction vs n_s relationship across the full range of starter cells (Fig 4A, S12A).

We aimed to estimate the number of starter cells beyond which one can consider the horizontal asymptote of the area input fraction vs n_s relationship to have been reached, and thus resulting in n_s invariant area input fraction values. To determine this threshold, we looked for a structural break in the area input fraction vs n_s curves, which would manifest itself as linear regressions on each side of the breakpoint having significantly different slopes [37]. We tested multiple break point values and found that 200 starter cells was the lowest value beyond which the number of areas showing a statistically significant difference for slopes reached its minimum (Fig S12B). Furthermore, the distributions of area-wise slopes from the linear regressions below or above the 200 starter cell cut-off were significantly different ($p= 0.03$, paired t-test). Importantly, slope values were close to zero for starter cell numbers above 200 (Fig 4C), confirming that in this range, the input fraction does not depend on n_s.

We have also examined the relationship of the convergence index to n_s. It displayed higher variability for low n_s values and asymptotic convergence at high n_s values (Fig S 13), similarly to area input fraction values. In addition, although all area convergence index vs n_s curves are initially decreasing, the absolute convergence index values for low

n_s have more apparent inter-area variability (Fig S14B). This is because the absolute convergence index value is dependent on the area size and not influenced by the relative growth of other brain areas.

To further illustrate how the range of sampled n_s can hinder comparisons of input maps by affecting input patterns and variability, we compared area input fractions calculated for a low and a high n_s group with equal number of observations. Statistical differences in area input fractions between the low- and high starter groups were found in 5 out of the 19 input areas analyzed (Fig S14A). In addition, data from the low starter group showed a much larger variability than the high starter group. Therefore, comparisons using the area input fraction measure should only be used for data sets where starter cell numbers are above the breakpoint value for which the area input fraction vs n_s relationship reaches its horizontal asymptote. Convergence index suffers even more drastically from larger variability in the low-starter group (Fig S14B) and using it to compare datasets with different n_s is inappropriate by construction.

2.4 Estimating the number of inputs for a single starter cell

It follows from the analysis above that area input fractions calculated from experiments using a population of starter cells cannot be interpreted at the level of individual starter neurons. However, the y-intercept of the $\log(n_i)$ vs $\log(n_s)$ relationship (Table 7) represents, once converted to linear scale, the number of input cells per starter cell. Using this procedure for individual input areas, we can then calculate the area input fractions for a single starter cell (Fig S15). The difference between the two measures is further highlighted by ranking the input areas according to their input fraction (Fig S15C).

Furthermore, as the y-intercept of the $\log(n_i)$ vs $\log(n_s)$ relationship is independent of the starter cell number range, it provides an adequate measure to compare different starter cell populations. To illustrate this, we calculated area input fractions for starter areas VISp and VISpm using the whole range of starter cells (Fig S16A) or using only experiments with starter numbers above 200 (Fig S16B). These measures then can be compared to the y-intercept method (Fig S16C). Differences apparent in the whole starter range comparison (Fig S16A) are driven by unequal slopes across input areas and as such are likely to be misleading. Consequently, a comparison using high starter numbers shows no area to be statistically different between VISp and VISpm (Fig S16B), whereas when using all starters area AM shows a statistically significant difference between VISp and VISpm. Comparisons using y-intercept values however revealed 2 significantly different areas (AM, VISl). The three methods thus provide markedly different results and we argue that only the y-intercept based approach can be interpreted at the level of single starter cells.

2.5 Relative connection probability determines the behaviour of area input fractions at low starter numbers

In order to directly assess how connectivity parameters affect the behaviour of the area input fraction vs n_s relationship, we simulated a network with 5 input areas using the probabilistic model introduced in Fig S3. Across the input areas, we either varied only the connection probability p (Fig 5), only the input pool size N_i (Fig S17), or both (Fig S18).

When only p was varied between input areas, the area input fraction varied with

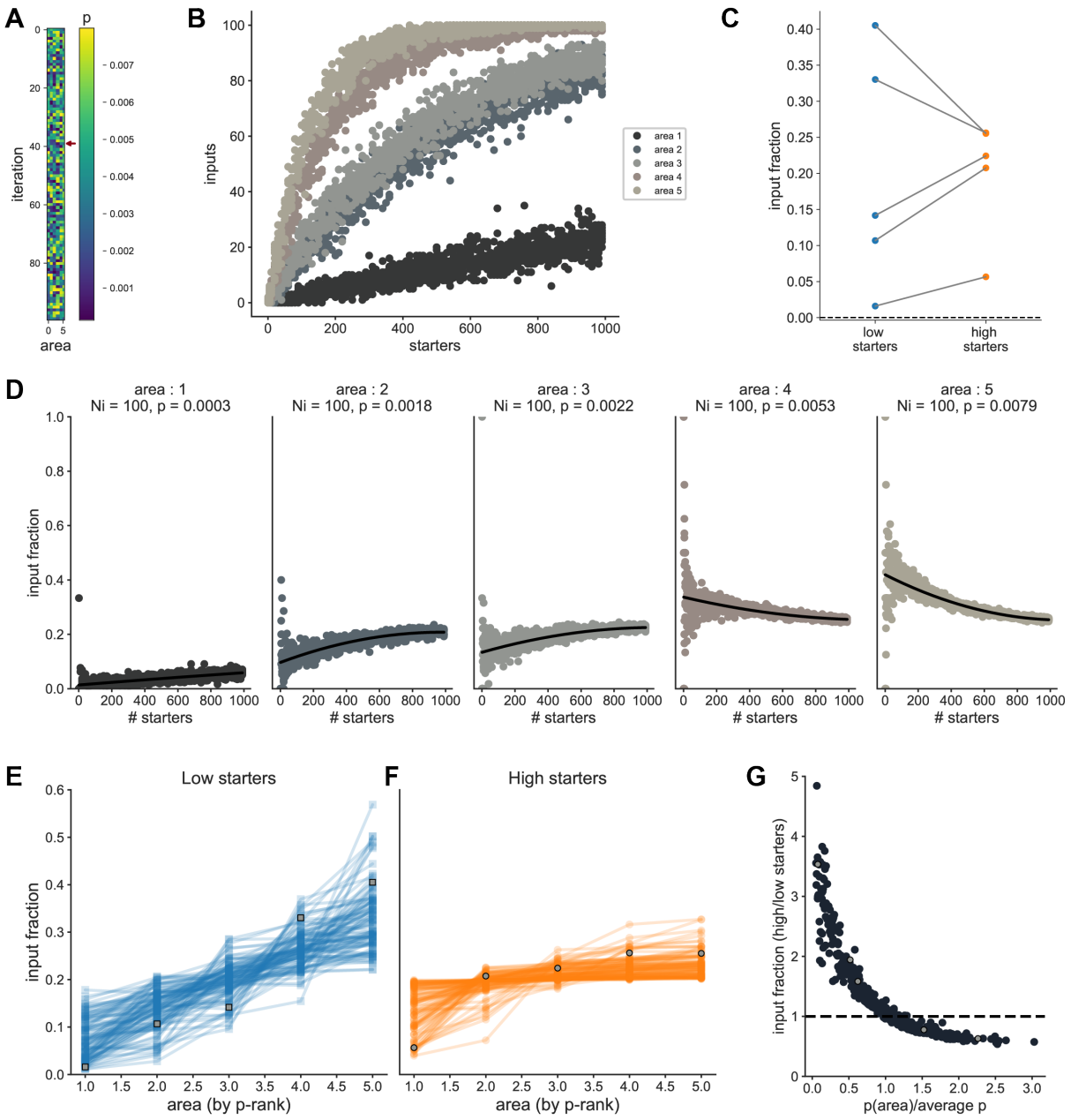

Figure 5: **Effect on relative connection probability on area input fraction vs starter relationship** Using the probabilistic model, we simulated 5 input areas, all with $N_i = 100$. 100 independent simulations were repeated to assess the effect of p. For each simulation, the connection probability p_i for each input area was randomly drawn between 10^{-4} and $8 * 10^{-3}$. (A) Heatmap showing the combination of connection probabilities used for each simulation. The simulation shown in plots B-D is indicated by a red arrow. (B) n_i vs. n_s relationship for all input areas for one example simulation. (C) Area input fraction for low starter numbers (lowest 10%) or for high starter numbers (highest 10%). (D) Area input fraction vs n_s relationship for each area. Black line is a polynomial fit. (E-F) Area input fraction vs rank of connection probability for low starters (E) or high starters (F). Data from the simulation plotted in B-D are shown in grey. (G) Relationship between the ratio of the area input fraction for high vs low starters, and the normalized connection probability per area. Data from the simulation plotted in B-E are shown in grey.

n_s, as in the experimental dataset (Fig5A-D). The influence of p on area input fractions vs n_s is more apparent for low starter cell numbers: areas with the highest connection probability are over-represented in terms of their relative input proportion, while areas

with lowest connection probabilities are under-represented (Fig5D, E). For high n_s, there is little dependence of area input fractions on p, since the area input fraction vs n_s relationship has reached its horizontal asymptote (Fig5D, F). This can be summarized by the decline of the relative input fraction between high and low n_s as a function of normalized p (Fig5G). In contrast, when only N_i was varied across input areas, the area input fraction for each area was constant across the starter cell range (Fig S17). Consequently there was no difference in area input fractions between low and high n_s datasets (Fig S17C,F). When both N_i and p were varied, the interaction remained essentially the same (Fig S18), i.e. p drove the difference between low and high n_s datasets.

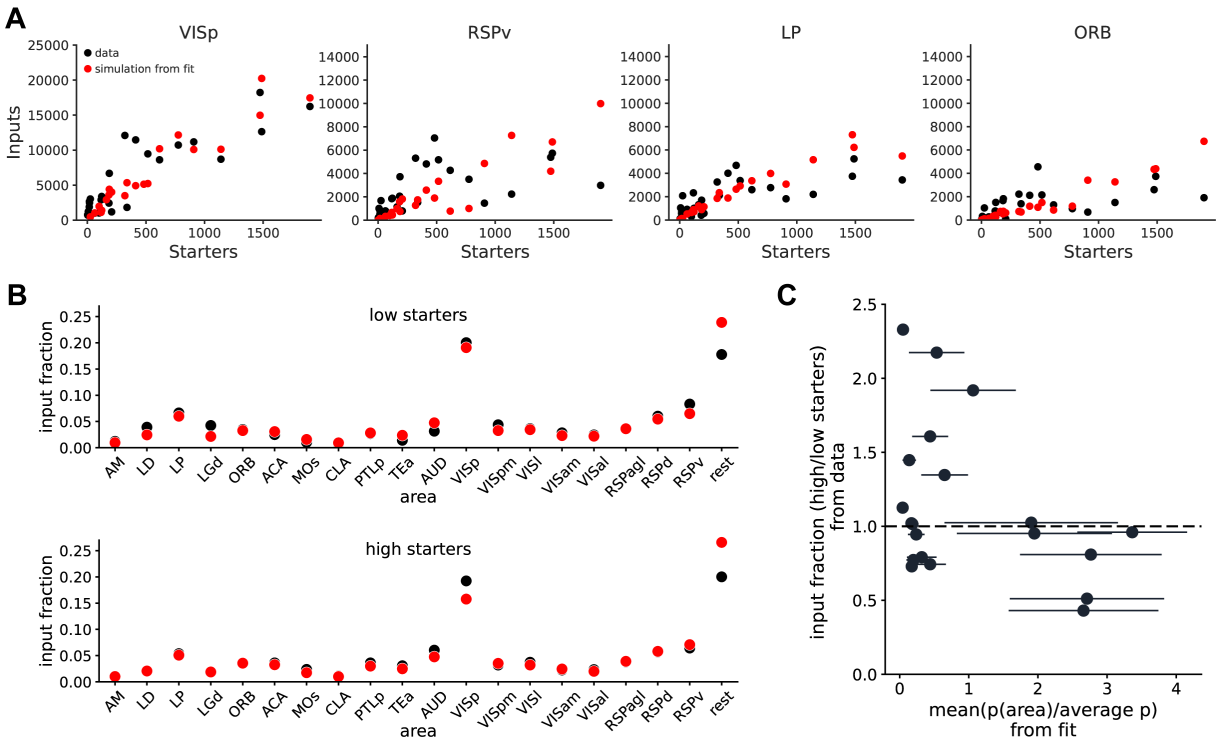

Figure 6: **Estimation of N_i and p per area in experimental dataset** (A) Four example areas with input vs starters relationships for the data (black) or simulations with parameters obtained from the model fit of the data (red), for one iteration of the fit. (B) Plot of experimental input fraction ratio between high and low starters vs relative p across areas obtained from fitting values

Finally, in order to obtain an estimate of N_i and p for input areas in our dataset, we fit the data using the likelihood function of the probabilistic model used for simulations. The fitting procedure was performed using maximum likelihood estimation, and returns fitted parameter values for N_i and p (Table 8). Using these values, we can then perform simulations using the same range of starter cells as the experimental data, and observe a good correspondence between experimental and simulated values (Fig 6A, Fig S19). The plot of area input fractions according to starter cell numbers (low or high starters, respectively Fig 6B top and bottom) reveals very similar trends in fitted and experimental datasets. Given the strong link between relative p and relative area input fraction between high and low n_s (Fig5E, F), the results of this simulation show that the relative value of p per area gets well captured by the multi-area fit of the model (6B cf. 5G).

3 Discussion

3.1 Experimental caveats

There are several technical caveats concerning the labelling and detection of neurons. Regarding labelling, we have used two helper viruses: one expressing the TVA-receptor and EGFP, and one expressing the G-protein but no fluorophore. The modified rabies virus was expressing mCherry. Neurons co-expressing EGFP and mCherry were thus defined as starter cells. However, this may result in neurons counted as starter cells but deficient in G protein, thus leading to an over-estimation of starter cells. Conversely, G protein only expressing neurons could become retrogradely infected through local connections and propagate rabies labelling to a second layer of monosynaptically connected neurons, thus leading to an overestimation of local input cells. We attempted to mitigate these confounds by injecting a mixture of high titre (˜10^{14} genome-copies/ml) helper viruses thus optimising for co-infection [38]. Regarding labelling by rabies virus, it is unknown if all connections have the same probability of propagation or not and our method is unable to distinguish between connection and propagation probability. Trans-synaptic spread depends on the presence of rabies virus receptors [39], is modulated by activity [40] and likely by the number and size of synaptic contacts between given input and starter cells. Future work is required on virus strains with enhanced neurotropism, on the identity of rabies receptors and on quantitative evaluation using orthogonal methods such as dense anatomical reconstruction allowing unequivocal identification of synaptic connections.

3.2 Cell counting

Some of the external datasets analysed in Fig S1 were quantified by counting labelled cells in separate brain slices. This approach can introduce bias and be a further source of variability. While advances in design-based stereological methods have improved cell number estimations from tissue slices [41], they typically rely on uniform cell densities and are rarely applied when quantifying rabies tracing data. To illustrate the problem, we have run numerical simulations using a range of biologically relevant cell densities (see methods). Counting cells in every slice or every 2^{nd}, 3^{rd} or 4^{th} slice consistently resulted in varying degrees of systematic overestimation (Fig S20). Furthermore, the variance between individual experiments was considerable, especially toward low cell densities. To further illustrate the problem using real data, we have virtually sectioned two brains from our dataset and counted cells in every 4^{th} slice. The estimated whole brain cell counts varied considerably depending on slice sampling. Importantly, estimates greatly differed from the cell counts obtained by whole-tissue 3D cell counting (Table 9). These results argue against estimating cell numbers by counting cells in sectioned tissue, especially when only sampling some slices. The imprecision introduced may underlie some of the model selection uncertainties in Fig S1. To achieve unbiased, accurate cell counts, cell counting in the whole 3D volume of interest is essential.

While automated 3D cell counting can deal with very large datasets and offers consistent results, systematic cell detection biases which scale with the label density cannot be excluded (e.g. under-detection at input areas with extremely high cell densities). However, this is unlikely to manifest in our results as model selection analysis is consistent across input areas with different label densities. In addition, datasets from multiple laboratories and acquired through different imaging and cell counting methods show the

same relationship. Interestingly, a dataset generated with no explicit cell counting, but rather quantifying projection volume by counting pixels reaching a certain fluorescence threshold (Allen Institute), shows a different residuals distribution (normal). Yet the n_i vs n_s relationship is still best described by a power-law relationship. The difference in residuals distribution analysis for this dataset may be expected through a presumably sub-linear increase and saturation in the projection volume with high cell densities. Additionally, an over-estimation for areas of low cell density is similarly expected, as the inclusion of neuropil has a disproportional effect at low cell densities.

Our results generalize well across external datasets, but it is important to note that the starter areas in all datasets explored here are cortical (except [34] and [32], which are from the olfactory bulb and amygdala, respectively). It remains to be determined how the n_i vs n_s relationship generalises to profoundly different neuronal structures, such as the cerebellum, striatum or the spinal cord.

3.3 Model selection and error structure

Metrics used in previous studies implicitly assumed linear scaling between the number of input and starter cells. We performed model selection analysis on our data (on whole brain inputs or area-defined inputs) and a range of external datasets, to compare the linear relationship with a range of candidate models that could describe the increase in number of inputs cells with increasing number of starter cells. For most datasets, the models with the lowest AICc values were the power-law and growth models (Table 1). This model selection analysis is limited by the data (both the number of observations, and the range of starter cells) and by the list of candidate models provided. For instance, although our dataset does not present any obvious saturation of the number of labelled inputs, one would expect a saturating regime to be reached if enough starter cells were labeled. Therefore this analysis does not aim at identifying a "true" underlying model, but at defining how to fit the data for consistent descriptive analysis. However, it does show that the linear model is consistently outperformed by competing non-linear models.

In addition, it is apparent that the n_i vs n_s relationships show a large variance in the data, and a skewed residuals distribution. The error structure analysis supports log-transformation of the data, which results in more normally distributed residuals (Fig 1 B, D). We thus performed further analysis after log-transformation.

Model selection on log-transformed data shows that a linear model provides a good description of the datasets. Although this doesn't represent the underlying model in log scale, it appears the range of n_s sampled corresponds to a linear part of the log-transformed dataset. We thus used a linear model for descriptive fitting.

3.4 Do rabies strains impact extracted parameters?

In recent years, viral tracing tools have considerably improved, thanks to the introduction of engineered glycoproteins [42] and more efficient rabies strains [6] that increased efficiency of synaptic transfer and reduced neuronal toxicity. One concern would be that using different rabies strains could lead to different n_i vs n_s relationship models. We analysed a large number of datasets comprising data from two different rabies strains (SAD-B19 or CVS-N2c), a large range of starter cell types and various starter areas. For the overwhelming majority of the datasets, our model selection analysis returned the same qualitative distribution (Tables 1, 2, 3 and Fig S1). We however did observe quan-

titative differences in $\log(n_i)$ vs $\log(n_s)$ relationships depending on the rabies strain used, with a higher intercept in the fit of the $\log(n_i)$ vs $\log(n_s)$ relationships for CVS-N2c. This is unsurprising given the improved retrograde transfer observed with this virus strain [6]. If the analysis introduced here is used to deduce connectivity parameters, or to compare them across different datasets, one should be mindful of the potential influence of the rabies strains used.

3.5 Effect of starter cell range on area input maps

In order to describe input maps obtained from rabies tracing experiments, inputs are typically either normalized to the total number of input cells in the same brain (area input fraction) or the number of starter cells (convergence index). We show directly that neither of these measures are independent of n_s (Fig S12, S13), and make comparisons between starter populations unreliable (Fig S14). The large and systematic biases are driven by two factors: first, the large variability of both measures at low starter cell numbers; and second, the different slopes of n_s vs area input fraction or convergence index for low and high n_s. Thus averaging either measure across the full range of n_s results in averaging across different behaviours. These biases are not surprising since neighbouring starter cells are likely to have some shared input cells.

The steepest non-linearity between area input fraction and number of starter cells is observed for small numbers of starter cells, before becoming close to constant for large numbers (Fig 4, S12A). Using data from experiments with n_s over which area input fractions are stable does mitigate this problem, yet the biological meaning of such derived area input fractions are far from trivial. As area input fractions are driven by the ensemble of different input areas, quantitative comparisons between populations with different input areas cannot be interpreted. However, these experiments do offer descriptive power and valuable qualitative insight of the census of input areas. For populations that share input areas to a large extent (e.g. starter populations with largely overlapping dendritic fields), quantitative comparison can be valid. In this case, area input fractions in a range independent of n_s show the relative propensity of a given input area to contact starter cells in the target region. This can be particularly useful not only to compare different but intermingled starter populations, but especially to compare the connectivity of the same starter population across e.g. treatments or time [40, 43, 44].

If the high n_s data can be averaged to lead to meaningful area input fractions values under certain conditions, what can be inferred from low n_s experiments? We observe that while convergence index vs n_s relationships are always decreasing before reaching their constant value, input fraction vs n_s relationships depend on the relative growth of the area inputs with respect to total brain input, and can be therefore either increasing or decreasing in the low range of n_s values (Fig 4C). This behaviour of area input fraction vs n_s relationships for low n_s informs on the growth of input area fraction and thus the connectivity probability (p) of input areas relative to each other (Fig 5).

3.6 Biological meaning of parameters

Systematic exploration of the parameter space of the probabilistic model, followed by fitting the resulting $\log(n_i)$ vs $\log(n_s)$ relationships, revealed the relationships between y-intercept, slope, and the connectivity parameters of the model. First, we observed that for a given value of p, the mean intercept increases with N_i, while the slope varies little.

In contrast, varying p for a given value of N_i affects both the slope and intercept. Furthermore, increasing the average degree of the starter set (i.e. the number of connections received by individual starter cells) leads to a shift of the mean intercept towards higher values, with no effect on the slope. Increasing the average degree of the input set (i.e. the number of connections given by an individual input cell) on the other hand leads to a decrease in the mean slope value. This is consistent with the shifts in distributions of both starter and input degrees observed when varying N_i and p using the probabilistic model (Fig S8). Using these observations we can attach a biological meaning to some of these parameters.

The measured y-intercept translates into the number of input cells to a single starter cell - a measure otherwise only obtainable by single-cell initiated rabies tracing [1, 2]. Fitting our dataset yields a y-intercept of 3.2, thus we estimate ∼1860 rabies labelled input neurons per starter cell. While the efficacy and specificity of transsynaptic rabies transmission present significant unknowns discussed elsewhere [43], this is not a wholly unreasonable estimate given a recent study reporting 7500 synapses for L2/3 pyramidal cells [45] and assuming multiple synapses per connection. The proportional contribution of different input areas to a single starter cell can be derived from the area-wise y-intercept measures, but it is important to keep in mind that there is no trivial mapping between rabies labelling and functional input strength [43, 46].

The fit values for input pool size (N_i) represent the size of the population of presynaptic cells which can be connected to the starter cell population. Assuming individual input neurons to carry somewhat independent information, N_i informs about the possible input diversity arriving from a given area. Based on this analysis, MOs, ACA, RSPv and RSPd give the most diverse inputs to L5PNs across VISp and VISpm. Conversely, as the input pools of e.g. VISal, AM and LGd are small, these connections are likely to have less information capacity.

3.7 Conclusion and recommendations

When planning rabies tracing experiments, one should first consider the required conclusions to be drawn. In general, starter cells should always be counted and a significantly larger number of samples, in the order of tens, should be planned. Starter cell numbers should ideally cover a broad range (from single digits to thousands), with denser sampling in the low n_s. In addition, the starter cell population should be as homogeneous as possible. Experimental data thus obtained can be subjected to model selection, and used to estimate biologically pertinent parameters, such as y-intercept and N_i. If only a small number of experiments are feasible, one should aim for a large number of starter cells where area input fractions have less variability across experiments and are close to a steady state. Area input fractions can in this case be used to compare similar starter cell populations e.g. before and after treatment. However, this approach requires estimating the starter cell number range where area input fractions are stable, which is likely to be dependent on multiple factors, including starter cell type and rabies strain used.

Tracing synaptic connectivity using modified rabies viruses is a powerful method in the toolkit of neuronal cartography, especially so when interpreted correctly. Just like with any other experimental method, methodically different approaches are essential to validate the conclusions and results should not be taken as ground truth. On top of these general concerns, the number of starter cells needs to be considered carefully both when planning experiments and when analysing rabies-obtained input maps.

4 Methods

4.1 Animals and viruses

All animal experiments were prospectively approved by the local ethics panel of the Francis Crick Institute (previously National Institute for Medical Research) and the UK Home Office under the Animals (Scientific Procedures) Act 1986 (PPL: 70/8935). The following transgenic mice on a C57BL/6 background were used: Tg(Colgalt2-Cre)NF107Gsat (RRID: MMRRC_036504-UCD, also known as Glt25d2-Cre); Tg(Rbp4-Cre)KL100Gsat/Mmucd (RRID: MMRRC_031125-UCD); Tg(Tlx3-cre)PL56Gsat (RRID: MMRRC_041158-UCD). Animals were housed in individually ventilated cages under a 12 hr light/dark cycle.

EnvA-CVS-N2cΔG-mCherry rabies virus, and adeno-associated viruses expressing TVA and EGFP (AAV8-EF1a-flex-GT) or CVS-N2c glycoprotein (AAV1-Syn-flex-H2B-N2CG) were a generous gift from Molly Strom and Troy Margrie. The AAV-EF1a-Cre plasmid (Plasmid #55636) and retrograde AAV2-retro helper vector (Plasmid #81070) were purchased from Addgene and generously packaged by Raquel Yustos and Prof. Bill Wisden at Imperial College London.

4.2 Surgical procedures

Surgeries were performed on mice aged 5-12 weeks using aseptic technique under isoflurane (2–3 %) anaesthesia, and analgesia (meloxicam 2 mg/kg and buprenorphine 0.1 mg/kg). The animals were head-fixed in a stereotaxic frame and a small hole (0.5–0.7 mm in diameter) was drilled in the skull above the injection site. The virus solution was loaded into a glass microinjection pipette (pulled to a tip diameter of 20 μm) and pressure injected into the target region at a rate of 0.4 nl/s using a Nanoject III delivery system (Drummond Scientific). To reduce backflow, the pipette was left in the brain for approximately 5 min after completion of each injection.

For rabies virus tracing experiments using cre driver lines a 1:2 mixture of TVA and CVS-N2c glycoprotein expressing cre-dependent AAVs (5-20 nL) was injected at stereotaxic coordinates (VISpm: lambda point - 0.8 mm, ML 1.6 mm, DV 0.6 mm; VISp: lambda point – 1.0 mm, ML 2.5 mm, DV 0.6 mm). For the TRIO experiments, 50 nL AAVretro-Ef1a-Cre was injected into LP (lambda point – 1.7 mm, ML 1.5 mm, DV 2.4 mm) followed in 3-8 weeks by the injection of helper AAVs as described above. Rabies virus (50-100 nL) was injected 5-7 days later at the same site. Ten to twelve days later, animals were transcardially perfused under terminal anaesthesia with cold phosphate-buffer (PB, 0.1 M) followed by 4 % paraformaldehyde (PFA) in PB (0.1 M).

4.3 Data acquisition and analysis

Brain samples were embedded in 4-5 % agarose (Sigma-Aldrich: 9012-36-6) in 0.1M PB and imaged using serial two-photon tomography [47, 48]. Eight optical sections were imaged every 5 μm with 1.2 μm x 1.2 μm lateral resolution, after which a 40 μm physical section was removed using a vibrating blade. Excitation was provided by a pulsed femto-second laser at 800 or 930 nm wavelength (MaiTai eHP, Spectra-physics). Images were acquired through a 16X, 0.8 NA objective (Nikon MRP07220) in three channels (green, red, blue) using photomultiplier tubes. Image tiles for each channel and optical plane were stitched together using the open-source MATLAB pack-

age StitchIt (https://github.com/SainsburyWellcomeCentre/StitchIt). For 3D cell detection the open-source package *cellfinder* [28] was used. Registration to the Allen CCFv3 [27])and segmentation was done using the *brainreg* package [17]. Cell coordinates were downsampled to 10 μm to match the resolution of the Allen CCFv3 space and the number of cells was counted for each segmented area. To reduce the occurrence of false positives, the hindbrain areas (HB) were removed from the whole brain cell counts, as these areas are known not to project directly to the neocortex.

Area-wise cell count data were imported into Python 3.6 and all further analysis performed using custom scripts. In the following Methods sections, we refer to n_s as the number of starter cells, and n_i as the number of input cells, or $n_{i,A}$ for the number of input cells in area A. For fitting relationships, the explanatory variable x can refer to n_s or $\log(n_s)$, and the dependent variable y can refer to n_i or $\log(n_i)$.

Cell counts for all experiments and the code used for analysis and generating figures can be found at `https://github.com/ranczlab/Tran_Van_Minh_et_al_2023`.

4.4 Descriptive statistics and model selection

The relationship between number of input cells and number of starter cells was fitted with multiple models using the *lmfit* package. The of candidate models used for model selection are : linear model, quadratic model, power-law model, exponential model, and a growth model defined by the equation :

$$y = \frac{y_{max} * x}{k + x}$$

For each model the Akaike Information Coefficient corected for small sample size (AIC_c) can be calculated as:

$$AIC_c = 2k + n\log(\frac{RSS}{n}) + \frac{2k(k+1)}{n-k-1}$$

where n is the sample size, k is the number of parameters of the model. The AIC_c for different models were compared, and if the difference in AIC_c values for two models is larger than 2, the model with the lowest AIC_c is considered to have better support [49].

4.5 Analysis of residuals distribution

If the residuals from a fit of the untransformed dataset follow a normal distribution, further analysis should be performed the untransformed dataset. If residuals follow a log-normal distribution, it is more appropriate to perform further analysis on log-transformed data. We used the method described in [31] to determine the error structure of the dataset. Briefly, we calculated the likelihood that the data is generated from a normal distribution with additive error:

$$\mathcal{L}_{norm} = \prod_{i=1}^{n}[\frac{1}{\sqrt{2\pi\sigma_{NLR}^2}}\exp(\frac{-(y_i - a_{NLR}x_i^{b_{NLR}})^2}{2\sigma_{NLR}^2})]$$

and the likelihood that the data is generated from a lognormal distribution with multi-

plicative error:

$$\mathcal{L}_{lognorm} = \prod_{i=1}^{n} [\frac{1}{\sqrt{2\pi\sigma_{LR}^2}} \exp(\frac{-(\log(y_i) - log(a_{LR} x_i^{b_{LR}}))^2}{2\sigma_{LR}^2})]$$

where n is the sample size. The $AICc$ for each error model was then calculated as:

$$AIC_c = 2k + n\log(\mathcal{L}) + \frac{2k(k+1)}{n-k-1}$$

and the two models with the lowest AIC_c value considered as having better statistical support if the difference in AIC_c values is larger than 2.

4.6 Estimation of fit parameters

In order to estimate the distribution of fit parameters for the $\log(n_i)$ (y) vs $\log(n_s)$ (x) relationships, we used residuals resampling. Briefly, for each bootstrap iteration i, a linear model was fit to the data to obtain fitted values $\hat{y}_i$ and residual values ϵ_i. The new values to fit were obtained by adding to a randomly resampled residual value from the initial fit ($y_{B,i} = \hat{y}_i + \epsilon_{i,j}$). The linear model was fit to this iteration. This step was repeated 5000 times and the resulting fits analyzed to obtain the confidence intervals of the fit parameters.

4.7 Probabilistic model

We modeled unidirectional connections between input areas I_a of size N_{i_a} and a starter area S of unspecified size. p_{I_a} is the probability that a neuron in area I is connected to a neuron in area S. For each observation, we sample N_s cells from the starter area, and build for each input area the adjacency matrix of size (N_{i_a}, N_s) that represents the connections between all N_{i_a} neurons and all N_s neurons. Each element $m_{i,j}$ of the adjacency matrix can take as values 0, if the i-th neuron of area I_a is not connected to the j-th neuron of area S, or 1 if the neurons of this pairs are connected, with $P(m_{i,j} = 1) = p_I$. Rabies tracing experiments were simulated by building an adjacency matrix per observation of the inputs vs starter graph, and repeating these observations over a similar range of starter numbers as a typical rabies experiment. Brain-to-brain variability was represented by sampling, for each observation, the model parameters from discretized normal distributions, truncated to keep only positive numbers, with specified mean and standard deviation.

4.8 Effect of the number of starter cells on area input fraction

Area input fractions were defined as the ratio between the number of cells in each input area in ipsilateral side, and the total inputs counted in the same brain. We use a Chow test [37] to test for structural breaks in the slope of the area input fraction vs starters relationships.

Multivariate linear regression analysis was used to compare the relative effect of starter cell numbers, starter cell locations, and starter cell genotype, on area input fractions for all regions of interest. The regression models were defined using the *ols* function

from the *statsmodel* Python package. Models with different combinations of the predictors were also assessed. Statistical significance of the models were assessed by an F test and all p values corrected for multiple comparisons using the Benjamini-Hochberg method. The predictors used were the starter cells number, genotype, and their location, represented by the target frac parameter. Because of the close proximity of the targeted injection locations (VISp and VISpm) for infection of starter cells, some brains had starter cells in both targeted areas. We scaled the ratio of starter cells in either area to represent the continuum between brains for which all starter cells are in VISp (corresponding to a target frac value of 1) and brains where all starter cells are in VISpm (target frac value of -1).

4.9 Bipartite configuration model

The adjacency matrices generated by the simulations define bipartite graphs, made of two sets of respectively N_i and N_s nodes. The degree of a node n corresponds to the number of edges connecting this node to the rest of the network. In order to assess the effect of the degree of each set on the fit parameters of the N_i vs N_s relationship, we built graphs of specified degrees distributions using the *bipartite_configuration_model* generative model function from the *networkx* package.
The degree distribution of the starter set was sampled from a normal distribution centered around its chosen average degree. Degrees of the corresponding input set are then picked iteratively from a normal distribution centered around its chosen average s degree, so that the sum of starter and input degrees are equal.

4.10 Analysis of the relative effects of connection probability and input pool sizes on area input fraction

In order to assess the effect of each model parameter on area input fractions, we used the probabilistic model to simulate 5 input areas and varied parameters independently. To assess the effect of connection probability, p_{I_a} for each area was randomly drawn between 10^{-4} and $8 * 10^{-3}$, and N_{i_a} set to 100. To assess the effect of input area size, N_{i_a} was a discrete value randomly picked between 100 and 500, and all p_{I_a} were set at $5{*}10^{-4}$. We also considered the effects of varying both p_{I_a} and N_{i_a} within the same ranges. Simulations were performed for up to $N_s = 1000$ starter cells. We refer to data with N_s in the bottom 10% and top 10% of this range as low starters group and high starters group, respectively. For each input area, the area input fraction vs starter relationship was fit with a second degree polynomial equation.

4.11 Derivation of the probabilistic model and fit of experimental data

For the probabilistic model for a single input area of size N_I and connection probability p_I, the likelihood of observing n_i inputs for N_s sampled starters can be formulated as :

$$\mathcal{L}(N_I, p_I) = \frac{N_I!}{n_i!(N_I - n_i)!}((1 - (1 - p_I)^{N_s})^{n_i})(1 - p_I)^{N_s(N_I - n_i)})$$

or, for an ensemble of areas :

$$\mathcal{L} = \prod_a \frac{N_{I_a}!}{n_{i,a}!(N_{I_a} - n_{i,a})!}((1 - (1 - p_{I_a})^{N_s})^{n_{i,a}})(1 - p_{I_a})^{N_s(N_{I_a} - n_{i,a})})$$

where N_{I_a} and p_{I_a} are the area the input pool size and connection probability of area a, respectively.

This equation was used to fit the experimental data, using the *differential_evolution* algorithm from the *scipy* package for global optimization.

Bounds passed to the fitting function were calculated as follows. First, area volumes were downloaded from the Allen Mouse CCF (volumes at 25 μm isotropic resolution) using the Allen SDK. Number of neurons per area were deduced using neuronal cells densities per brain areas from [50,51]. If the density for a specific area was not specified in [50], we used the density for the next level up in the Allen hierarchy as a proxy. For N_i, lower and upper bounds were defined as 1/40 and 1/(1.5) of the number of estimated neurons per area, rounded up to the nearest thousand, respectively. For p, bounds were 1E-07 and 6.00E-04, respectively, for all areas expect the "rest of brain" area, for which bounds were 1.00E-08 and 1.00E-04. Bounds for all areas are listed in Table 10. The fit was performed 100 times with different seed values to assess the effect of initialization parameters.

The resulting N_{I_a} and p_{I_a} values for each area were then used with the probabilistic model to obtain the values plotted in Figure 6.

4.12 Classification of rabies strains across datasets

We used all datasets with starter cell identified as Pyramidal cells or interneurons and input cells quantified as cell counts. Classification was performed using the *sklearn* package. Rabies strain was used as the target of the classification, and cell type, starter numbers and input numbers used as features. Starter and input numbers were normalized using *MinMaxScaler*. Linear support vector classification was performed using the *LinearSVC* classifier. We used stratified k-fold cross-validation with k = 4. Briefly, the data was randomly divided into k subsets, so that the created folds preserve the distribution of classes observed in the complete dataset. Each subset was iteratively used as the test set while the other k-1 subsets were used for training. The resulting k classification scores were averaged to obtain a final score.

4.13 Cell counting artefacts in brain sections

First, we created 0.5 x 0.5 x 4 mm tissue blocks and randomly populated them with cells of 20 μm diameter in densities varying from 10 to 40000 cells / mm^3. Next, overlapping cells were removed, resulting in a final density range of 10 to 20000 cells / mm^3, the maximum corresponding to roughly 20% of total neuronal densities in mouse cortex [51]. We then simulated slicing the tissue block into 50 and 100 μm thick slices and counted cells in every slice, or every 2$^{\text{nd}}$, 3$^{\text{rd}}$ or 4$^{\text{th}}$ slice and multiplied the counts accordingly. We repeated these experiments 100 times and calculated the average ratio between the real cell numbers in the tissue block and the estimates.

5 Acknowledgements

We thank Troy Margrie and Molly Strom for viral constructs, Rob Campbell, Charlie Rousseau and Adam Tyson for help with data acquisition and analysis of rabies tracing experiments, Gavin Kelly for help with model selection, Marco Beato, Jonny Kohl and Petr Znamenskiy for comments on the manuscript, and all colleagues who shared their

data in Fig S1. For the purpose of Open Access, the author has applied a CC BY public copyright licence to any Author Accepted Manuscript version arising from this submission.

6 Tables

Table 1: **ΔAICc for untransformed data**
External datasets are from [13–15, 18, 19, 21, 22, 25, 32–36]. For easier comparison, we show the ΔAICc values, calculated as the difference between the AICc value for each model and the lowest AICc value per dataset. Lower AIC values indicate a better-fit model, and a model with a ΔAIC (the difference between the two AIC values being compared) of more than -2 is considered significantly better than the model it is being compared to.

dataset	rabies	linear	power-law	exponential	quadratic	growth
this dataset	CVS-N2c	10.75	**1.24**	17.60	20.44	**0.00**
Beier [19]	SAD-B19	23.66	10.00	30.93	19.97	**0.00**
Brown [22]	SAD-B19	4.26	2.20	4.26	12.02	**0.00**
Fu [32]	SAD-B19	**1.08**	**0.00**	18.17	14.42	**1.29**
Gehrlach [33]	SAD-B19	2.31	**1.04**	2.63	16.54	**0.00**
Graham interneuron [21]	CVS-N2c	**1.15**	**0.55**	14.79	15.74	**0.00**
Graham projection [21]	CVS-N2c	**0.29**	**0.00**	13.08	16.52	**0.91**
Hafner [18]	SAD-B19	**0.00**	**0.00**	9.13	17.94	**0.01**
Kim [25]	SAD-B19	4.00	**1.94**	4.75	11.53	**0.00**
Pouchelon P30-P42 [13]	CVS-N2c	2.75	**1.20**	5.93	14.15	**0.00**
Pouchelon P5-P10 [13]	CVS-N2c	**0.47**	**0.00**	28.94	15.85	**0.94**
Sun [14]	SAD-B19	32.32	14.48	**0.00**	23.80	36.58
Takatoh [36]	SAD-B19	**0.00**	**0.73**	4.00	15.58	**1.87**
Vinograd [34]	SAD-B19	**1.55**	**0.82**	**1.63**	17.19	**0.00**
Wee [15]	SAD-B19	2.72	**0.00**	5.62	17.55	**1.99**
Allen Institute [35]	CVS-N2c	7.16	**0.00**	17.17	14.32	3.58

Table 2: **ΔAICc for log-transformed data**

dataset	rabies	linear	quadratic
this dataset	CVS-N2c	**0.00**	15.99
Beier	SAD-B19	**0.00**	13.47
Brown	SAD-B19	**0.00**	11.97
Fu	SAD-B19	**0.00**	14.18
Gehrlach	SAD-B19	**0.00**	15.93
Graham interneuron	CVS-N2c	**0.00**	15.25
Graham projection	CVS-N2c	**0.00**	16.23
Hafner	SAD-B19	**0.00**	17.55
Kim	SAD-B19	**0.00**	13.43
Pouchelon - P30-P42	CVS-N2c	**0.00**	16.03
Pouchelon - P5-P10	CVS-N2c	**0.00**	16.15
Sun	SAD-B19	**0.00**	12.90
Takatoh	SAD-B19	**0.00**	16.34
Vinograd	SAD-B19	**0.00**	16.28
Wee	SAD-B19	**0.00**	15.70
Allen Institute	CVS-N2c	**0.00**	16.15

Table 3: **ΔAICc for residuals distribution**

dataset	rabies	log-normal	normal
this dataset	CVS-N2c	**0.00**	25.20
Beier	SAD-B19	**0.00**	189.86
Brown	SAD-B19	**0.00**	9.84
Fu	SAD-B19	**0.00**	7.81
Gehrlach	SAD-B19	**0.00**	7.52
Graham interneuron	CVS-N2c	6.33	**0.00**
Graham projection	CVS-N2c	**0.00**	2.39
Hafner	SAD-B19	**0.42**	**0.00**
Kim	SAD-B19	**0.00**	8.17
Pouchelon P30-P42	CVS-N2c	**0.00**	4.36
Pouchelon P5-P10	CVS-N2c	**0.00**	15.08
Sun	SAD-B19	**0.00**	24.50
Takatoh	SAD-B19	**0.00**	2.46
Vinograd	SAD-B19	**0.00**	4.66
Wee	SAD-B19	**0.00**	**1.02**
Allen Institute	CVS-N2c	6.59	**0.00**

Table 4: **ΔAICc for untransformed data for individual brain areas**

dataset	Linear	Power-law	Exponential	Quadratic	growth
VISp	5.91	**0.00**	16.33	16.35	**0.39**
VISpm	9.10	2.98	10.92	12.26	**0.00**
VISl	9.17	**0.61**	14.60	19.52	**0.00**
VISam	10.99	3.11	13.30	17.15	**0.00**
VISal	2.36	**0.00**	5.41	18.25	3.14
RSPagl	10.52	3.45	13.26	18.03	**0.00**
RSPd	8.90	2.07	12.44	17.95	**0.00**
RSPv	11.14	3.13	13.91	18.23	**0.00**
AM	11.57	3.96	13.27	21.18	**0.00**
LD	13.67	**0.00**	18.15	20.51	**0.48**
LP	7.68	**0.15**	12.03	17.53	**0.00**
LGd	**0.00**	**1.28**	**1.49**	16.08	6.12
ORB	7.32	**1.64**	9.80	19.40	**0.00**
ACA	7.41	2.03	10.75	19.83	**0.00**
MOs	**0.39**	**0.99**	**0.00**	15.40	**1.40**
CLA	5.80	**0.81**	9.43	19.91	**0.00**
PTLp	**1.00**	**0.00**	2.71	17.08	3.02
TEa	7.32	**0.85**	15.18	19.16	**0.00**
AUD	5.83	**0.00**	17.33	18.38	**1.30**

Table 5: **ΔAICc for log-transformed data for individual brain areas**

dataset	Linear	Quadratic
VISp	**0.0**	12.66
VISpm	**0.0**	16.08
VISl	**0.0**	14.44
VISam	**0.0**	14.18
VISal	**0.0**	16.03
RSPagl	**0.0**	16.06
RSPd	**0.0**	15.48
RSPv	**0.0**	15.79
AM	**0.0**	15.61
LD	**0.0**	15.13
LP	**0.0**	12.13
LGd	**0.0**	12.35
ORB	**0.0**	14.71
ACA	**0.0**	15.89
MOs	**0.0**	12.31
CLA	**0.0**	12.24
PTLp	**0.0**	15.88
TEa	**0.0**	15.79
AUD	**0.0**	16.05

Table 6: **ΔAICc for residuals distribution for individual brain areas**

dataset	log-Normal	Normal
VISp	**0.00**	5.42
VISpm	**0.00**	28.54
VISl	**0.00**	6.05
VISam	**0.00**	12.88
VISal	**0.00**	17.31
RSPagl	**0.00**	31.49
RSPd	**0.00**	26.24
RSPv	**0.00**	23.66
AM	**0.00**	9.54
LD	**0.00**	12.59
LP	**0.82**	**0.00**
LGd	**0.00**	**1.16**
ORB	**0.00**	26.22
ACA	**0.00**	44.72
MOs	**0.00**	35.05
CLA	**0.00**	40.35
PTLp	**0.00**	18.47
TEa	**0.00**	32.55
AUD	**0.00**	14.39

Table 7: **Intercept values from linear fits of log(n_i) vs log(n_s) relationships**

	all targets		VISp		VISpm	
	mean	CI95	mean	CI95	mean	CI95
area						
whole-brain	3.27	(3.09, 3.45)	3.28	(3.06, 3.49)	3.23	(2.75, 3.70)
VISp	2.62	(2.35, 2.85)	2.66	(2.36, 2.91)	2.32	(1.60, 2.93)
VISpm	1.96	(1.60, 2.28)	1.88	(1.53, 2.23)	2.28	(1.25, 3.03)
VISl	1.60	(1.27, 1.90)	1.37	(0.85, 1.83)	2.00	(1.62, 2.36)
VISam	1.55	(1.14, 1.90)	1.38	(0.83, 1.93)	2.01	(1.42, 2.49)
VISal	1.58	(1.31, 1.83)	1.47	(1.07, 1.85)	1.49	(1.10, 1.94)
RSPagl	1.75	(1.42, 2.04)	1.71	(1.32, 2.10)	1.86	(1.16, 2.50)
RSPd	1.98	(1.68, 2.27)	1.99	(1.63, 2.38)	2.20	(1.54, 2.77)
RSPv	2.22	(1.94, 2.47)	2.24	(1.92, 2.57)	2.40	(1.81, 2.94)
AM	1.10	(0.60, 1.50)	0.90	(0.21, 1.52)	1.71	(1.28, 2.14)
LD	2.01	(1.87, 2.17)	2.07	(1.89, 2.28)	2.16	(1.88, 2.43)
LP	1.73	(1.31, 2.11)	1.96	(1.50, 2.40)	2.47	(1.85, 2.93)
LGd	2.05	(1.71, 2.35)	2.10	(1.88, 2.32)	1.46	(0.60, 2.22)
ORB	1.55	(1.16, 1.90)	1.46	(1.03, 1.89)	1.81	(0.65, 2.62)
ACA	1.25	(0.95, 1.55)	1.12	(0.76, 1.52)	1.15	(0.54, 1.76)
MOs	0.88	(0.54, 1.20)	0.80	(0.34, 1.20)	0.37	(-0.34, 1.08)
CLA	0.55	(0.24, 0.86)	0.70	(0.34, 1.08)	0.71	(0.04, 1.30)
PTLp	1.32	(0.95, 1.63)	1.13	(0.61, 1.61)	1.47	(0.65, 2.14)
TEa	0.85	(0.54, 1.16)	0.80	(0.37, 1.25)	0.61	(0.05, 1.26)
AUD	1.35	(1.05, 1.64)	1.30	(0.76, 1.65)	1.28	(0.80, 1.86)

Table 8: **Parameters obtained from fitting the probabilistic model to experimental data** (from Fig 6)

	N_i		p	
area	mean	s.d.	mean	s.d.
VISp	3.63e+04	3.75e+04	5.83e-04	9.39e-05
VISpm	1.01e+05	1.28e+04	2.99e-05	7.73e-06
VISl	2.17e+04	2.37e+04	3.51e-04	2.41e-04
VISam	4.80e+04	2.09e+04	5.46e-05	3.30e-05
VISal	1.32e+04	1.56e+04	3.56e-04	2.13e-04
RSPagl	1.22e+05	3.09e+04	2.90e-05	1.13e-05
RSPd	1.40e+05	5.32e+04	4.05e-05	1.66e-05
RSPv	1.98e+05	6.24e+04	3.40e-05	1.57e-05
AM	1.26e+04	3.27e+03	7.48e-05	2.91e-05
LD	8.54e+03	1.20e+04	4.86e-04	2.02e-04
LP	1.51e+04	1.30e+04	4.91e-04	1.81e-04
LGd	6.07e+03	5.57e+03	4.72e-04	1.92e-04
ORB	1.13e+05	4.44e+04	3.13e-05	1.37e-05
ACA	1.50e+05	6.80e+04	2.37e-05	1.53e-05
MOs	2.68e+05	2.16e+05	8.26e-06	5.26e-06
CLA	1.45e+04	8.05e+03	7.61e-05	4.43e-05
PTLp	3.15e+04	2.25e+04	1.13e-04	5.44e-05
TEa	4.05e+04	3.39e+04	9.20e-05	6.43e-05
AUD	5.23e+04	6.54e+04	1.87e-04	1.09e-04
rest	6.90e+06	7.09e+06	7.41e-06	7.18e-06

Table 9: **2D detection artefacts.** Number of inputs from 2 brains using 3D detection or for simulated 2D detection from consecutive 50 μm wide slices, keeping every 4^{th} slice, assuming cell radii of 10 μm.

true number of inputs	slice 1 of 4	slice 2 of 4	slice 3 of 4	slice 4 of 4
49479	45068	66880	96336	64680
7785	5500	16480	15060	6576

Table 10: **Bounds per area for fitting the probabilistic model to experimental data** (from Fig 6)

	N_i		p	
area	min	max	min	max
VISp	2.70E+04	7.33E+05	1.00E-07	6.00E-04
VISpm	4.00E+03	1.08E+05	1.00E-07	6.00E-04
VISl	5.00E+03	1.27E+05	1.00E-07	6.00E-04
VISam	3.00E+03	8.20E+04	1.00E-07	6.00E-04
VISal	3.00E+03	7.80E+04	1.00E-07	6.00E-04
RSPagl	6.00E+03	1.54E+05	1.00E-07	6.00E-04
RSPd	9.00E+03	2.48E+05	1.00E-07	6.00E-04
RSPv	1.10E+04	2.85E+05	1.00E-07	6.00E-04
AM	1.00E+03	1.60E+04	1.00E-07	6.00E-04
LD	3.00E+03	6.80E+04	1.00E-07	6.00E-04
LP	3.00E+03	8.00E+04	1.00E-07	6.00E-04
LGd	1.00E+03	3.50E+04	1.00E-07	6.00E-04
ORB	7.00E+03	1.89E+05	1.00E-07	6.00E-04
ACA	1.10E+04	2.83E+05	1.00E-07	6.00E-04
MOs	4.40E+04	1.19E+06	1.00E-07	6.00E-04
CLA	1.00E+03	3.70E+04	1.050E-07	6.00E-04
PTLp	5.00E+03	1.25E+05	1.00E-07	6.00E-04
TEa	7.00E+03	1.91E+05	1.00E-07	6.00E-04
AUD	1.60E+04	4.24E+05	1.00E-07	6.00E-04
rest	5.00E+05	1.00E+08	1.00E-08	1.00E-04

7 Supplementary Figures

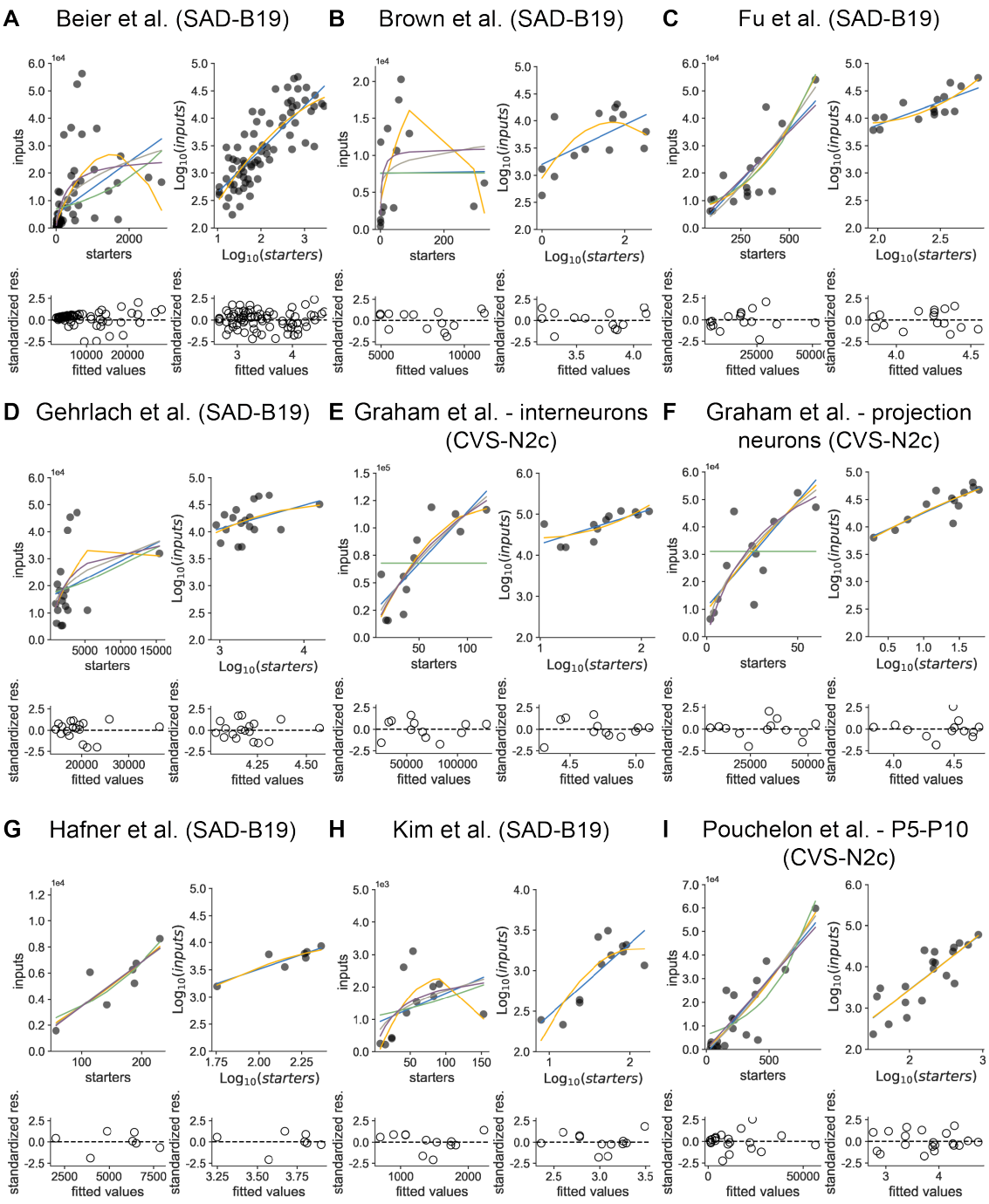

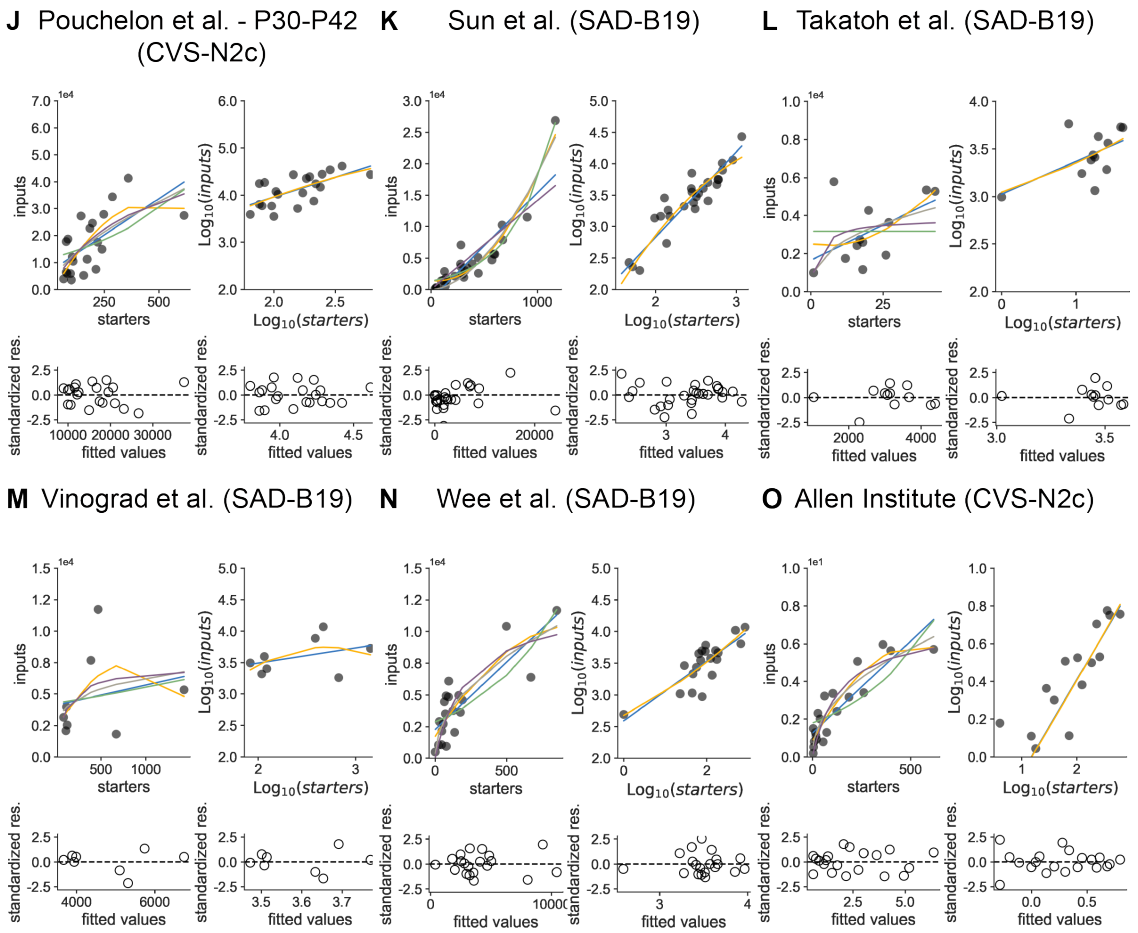

Figure S 1: **Model comparison for whole-brain data for other datasets.** Colours indicate different fitted models, with the same colour-code as in Figure 1. Datasets are from [13–15,18,19,21,22,25,32–36]. Please note that input quantification is done by counting labelled pixels instead of individual neurons in the Allen Institute dataset (panel O).

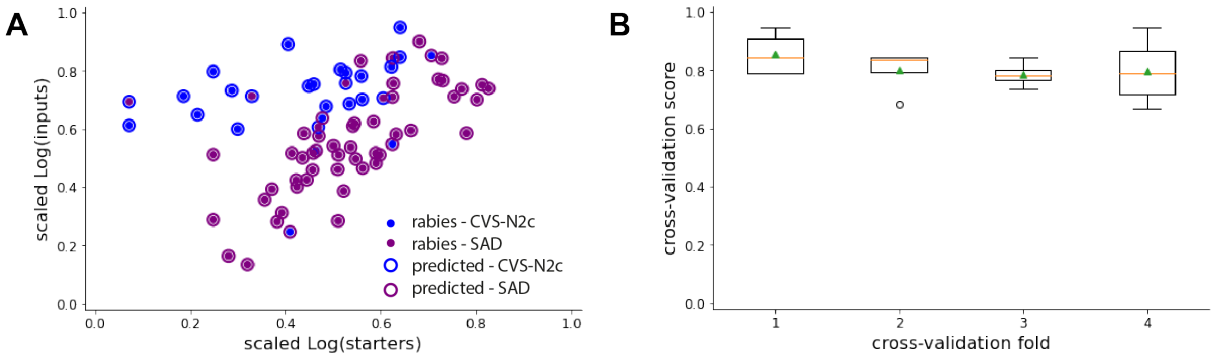

Figure S 2: **Classification of rabies strain in pooled datasets.** (A) Classification of the rabies strain used based on $\log(n_s)$, $\log(n_i)$ and starter cell type, for all pooled datasets where starter cell type was clearly identified as either pyramidal cells or interneurons and inputs quantified as cell counts. The model was a linear support vector classifier, and we used stratified 4-fold cross-validation to preserve the percentage of samples for each class. The plot corresponds to a single cross-validation fold. (B), Cross-validation scores show consistent accuracy across folds.

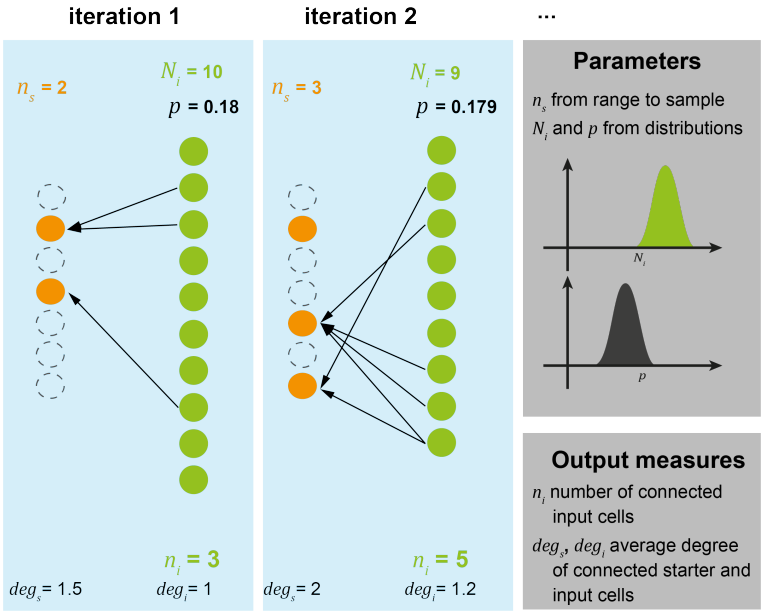

Figure S 3: **Probabilistic model.** Illustration of input parameters, iteration steps and output measures for the probabilistic model.

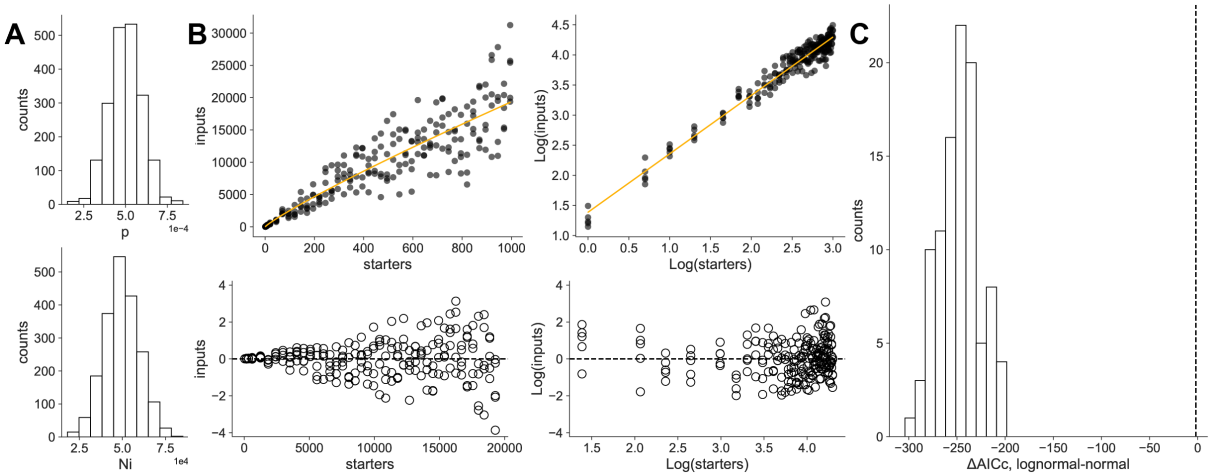

Figure S 4: **Variability in connectivity parameters leads to skewness of residuals.** (A) Distributions of connectivity parameters (p, average $5 * 10^{-4}$, and N_i, average 50000 cells; both distributions have a s.d. of 0.2 * their average value). (B) Simulation of inter area connectivity with the probabilistic model plotted as in Figure 1. Connectivity parameters are randomly drawn from the distributions in A for each observation. (C) Simulations as in B were performed 100 times and residual analysis was performed for each resulting curve. Dotted line represents dAICc of -2.

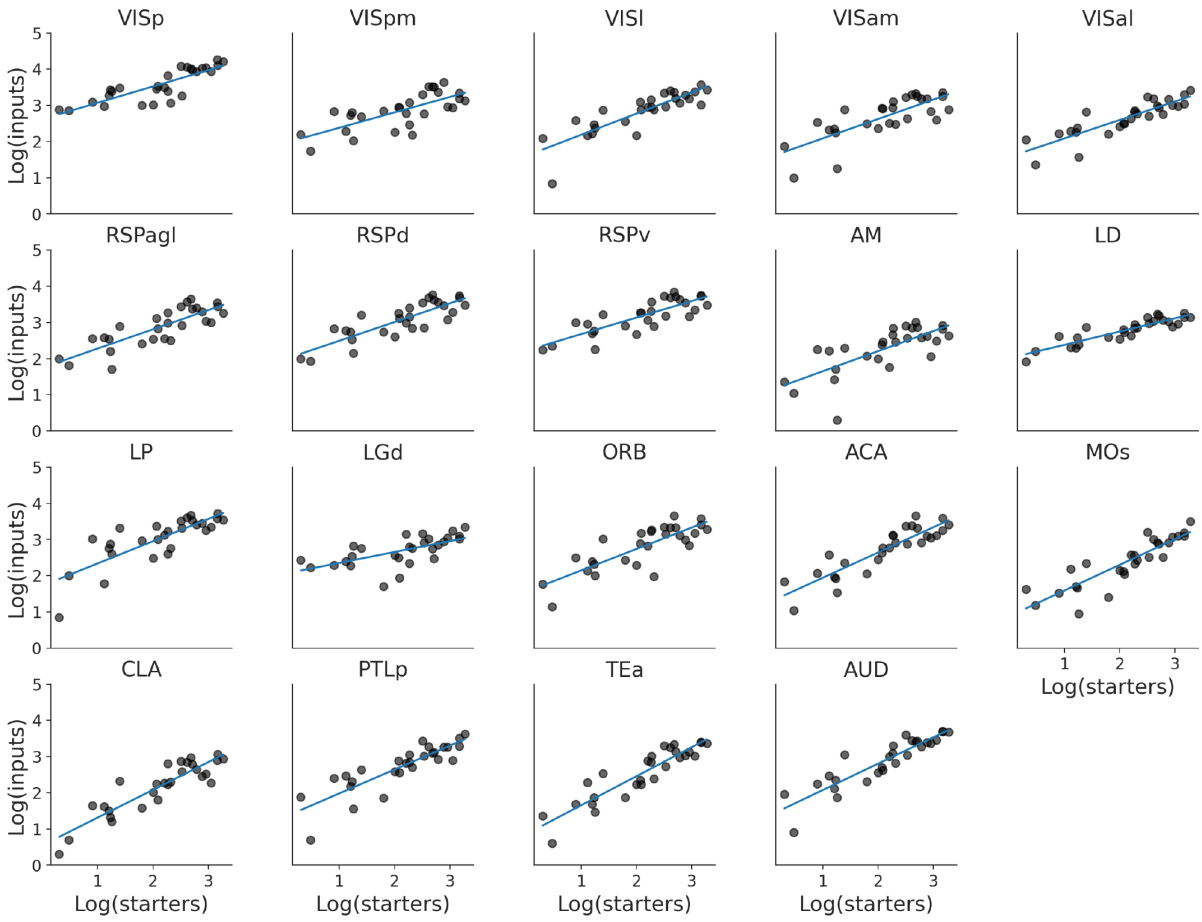

Figure S 5: **Linear fits per input area.** Linear fits of log-transformed n_i vs n_s relationship for individual brain areas.

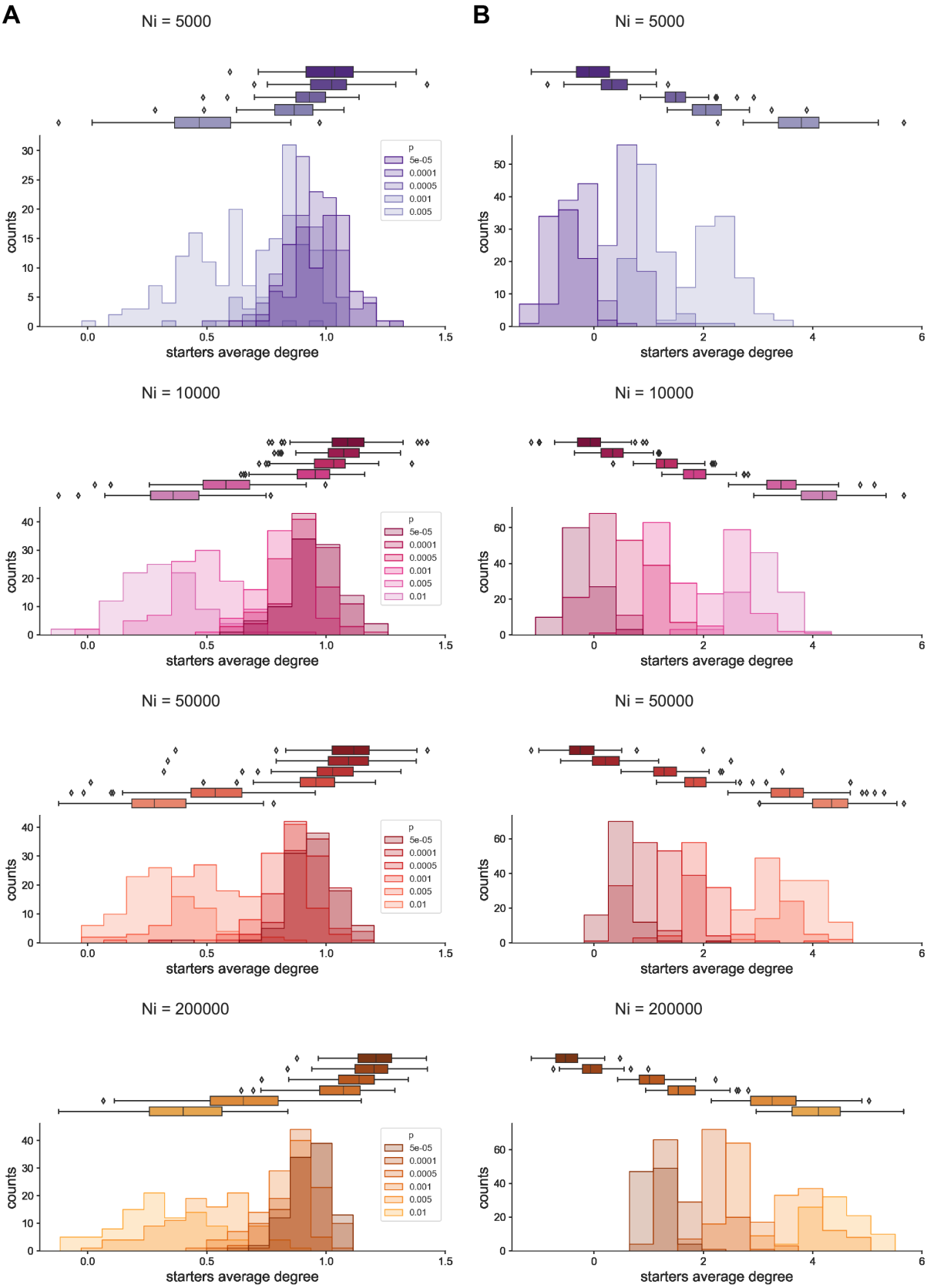

Figure S 6: **Distributions of fit parameters for log(n_i) vs log(n_s) relationships with varying N_i and p.** Distributions of slope (A) and y-intercept (B) values obtained across simulations with various model parameters (colours for N_i and shading for p), as plotted in Fig 2. Both N_i and p were drawn from distributions with a width of 0.2 * average.

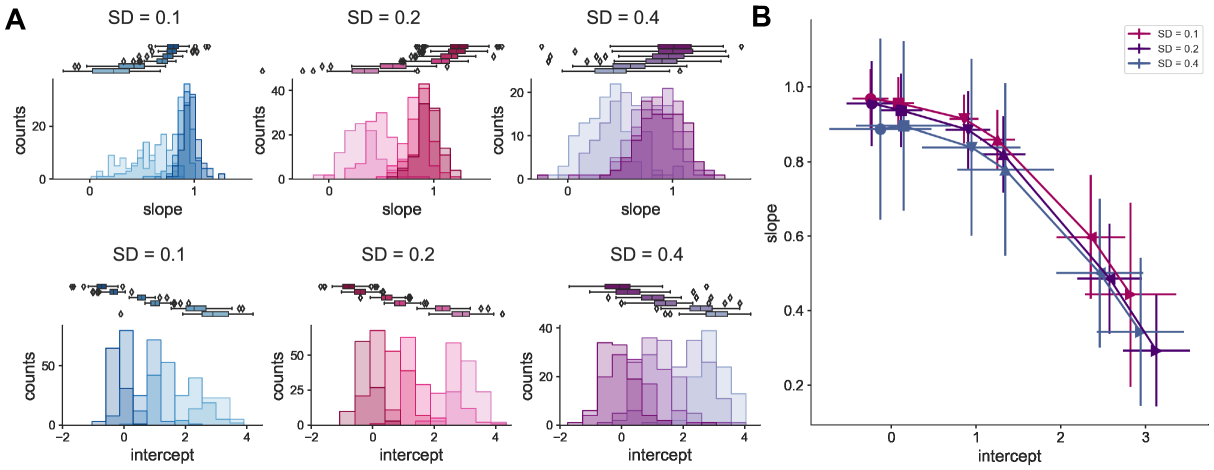

Figure S 7: **Varying the width of model parameter distributions has little effect on fit parameters of log(n_i) vs log(n_s) relationship.** (A) Distributions of fit parameters of log(n_i) vs log(n_s) relationship for an average $N_i = 10000$, varying connection probabilities as in Fig 2 and parameters drawn from distribution of varying widths (S.D. = 0.1, 0.2 or 0.4 * average). (B) Slope vs y-intercept plot for an average $N_i = 10000$ with both model parameters drawn from distribution of varying widths.

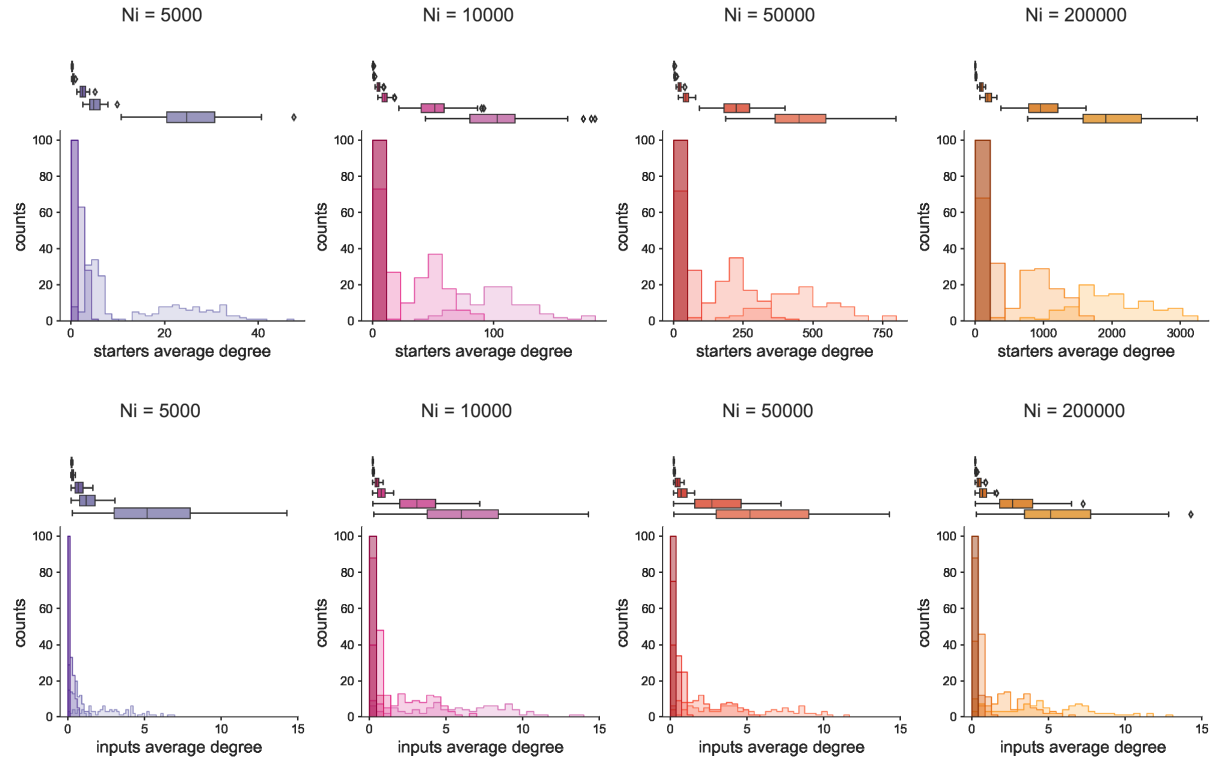

Figure S 8: **Degree distributions from simulations with the probabilistic model.** (Top) Distributions of starter cell degrees for varying N_i and p parameters. Both parameters were drawn from distributions of with 0.2 * average value of parameter. (Bottom) Distributions of input cell degrees for varying N_i and p parameters. Both parameters were drawn from distributions of with 0.2 * average value of parameter.

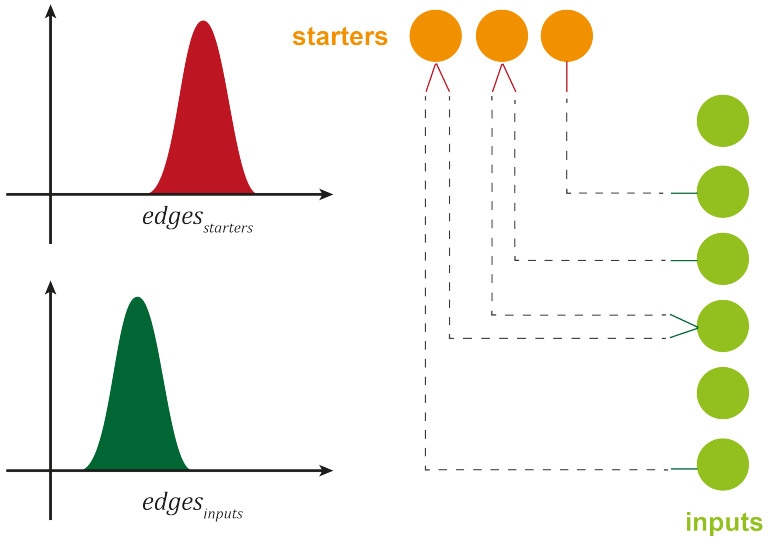

Figure S 9: **Configuration model.** Illustration of a single step of the simulations for the configuration model.

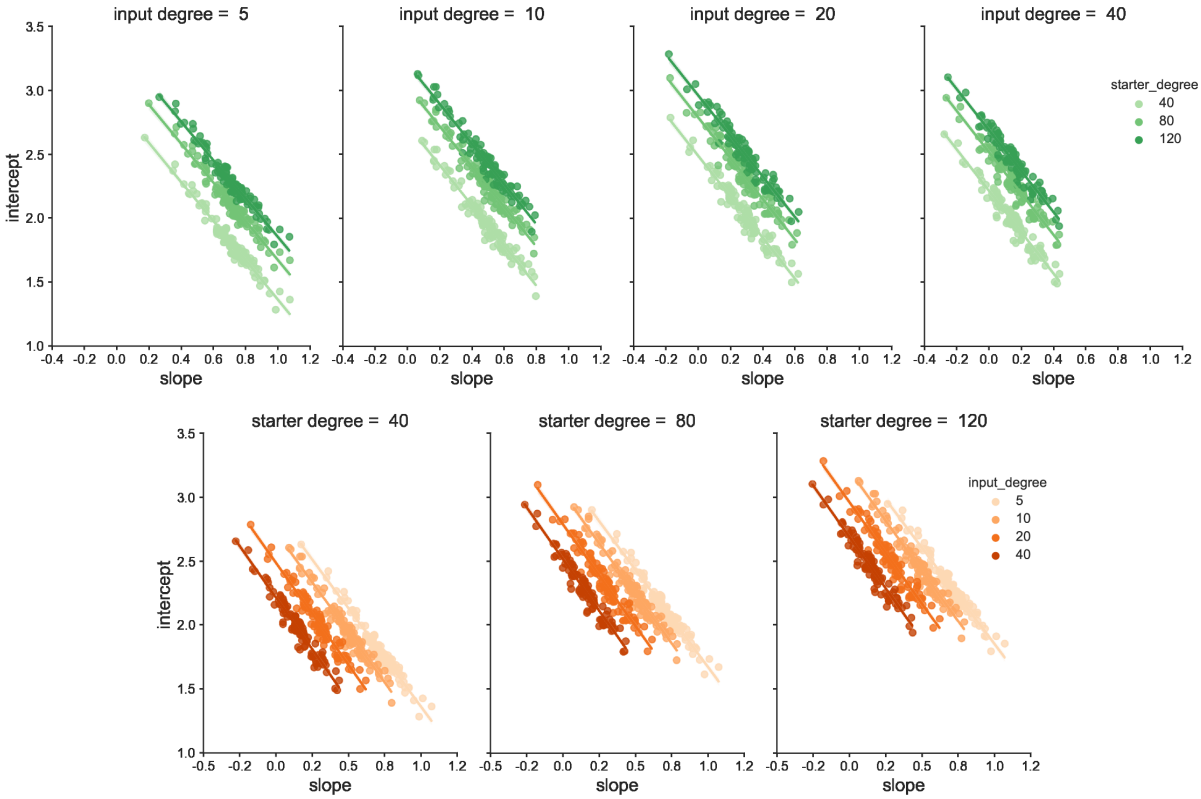

Figure S 10: **Intercept vs slope relationships in simulations using the configuration model.** (Top) Influence of starter degree on intercept vs slope relationships (each panel is a specified mean input degree). (Bottom) Influence of input degree on intercept vs slope relationships (each panel is a specified mean starter degree).

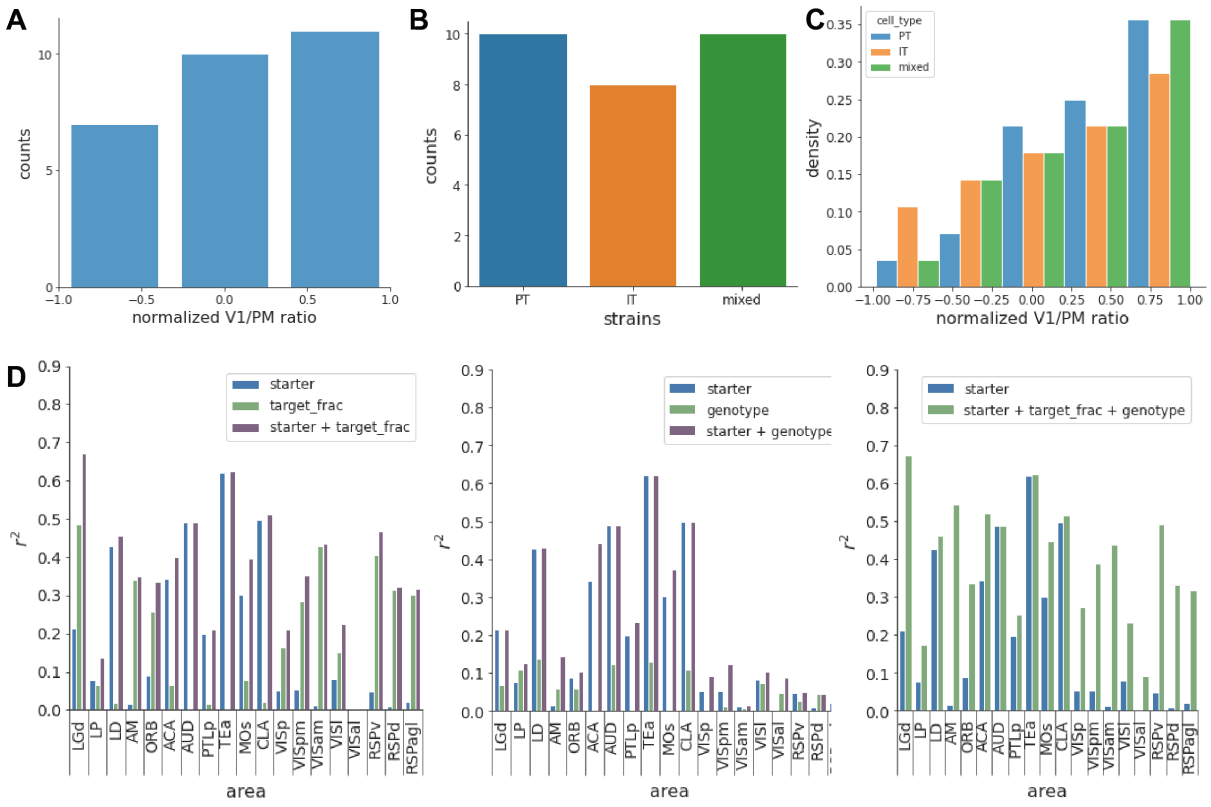

Figure S 11: **Multivariate linear regression of the area input fraction across areas using combined predictors.**

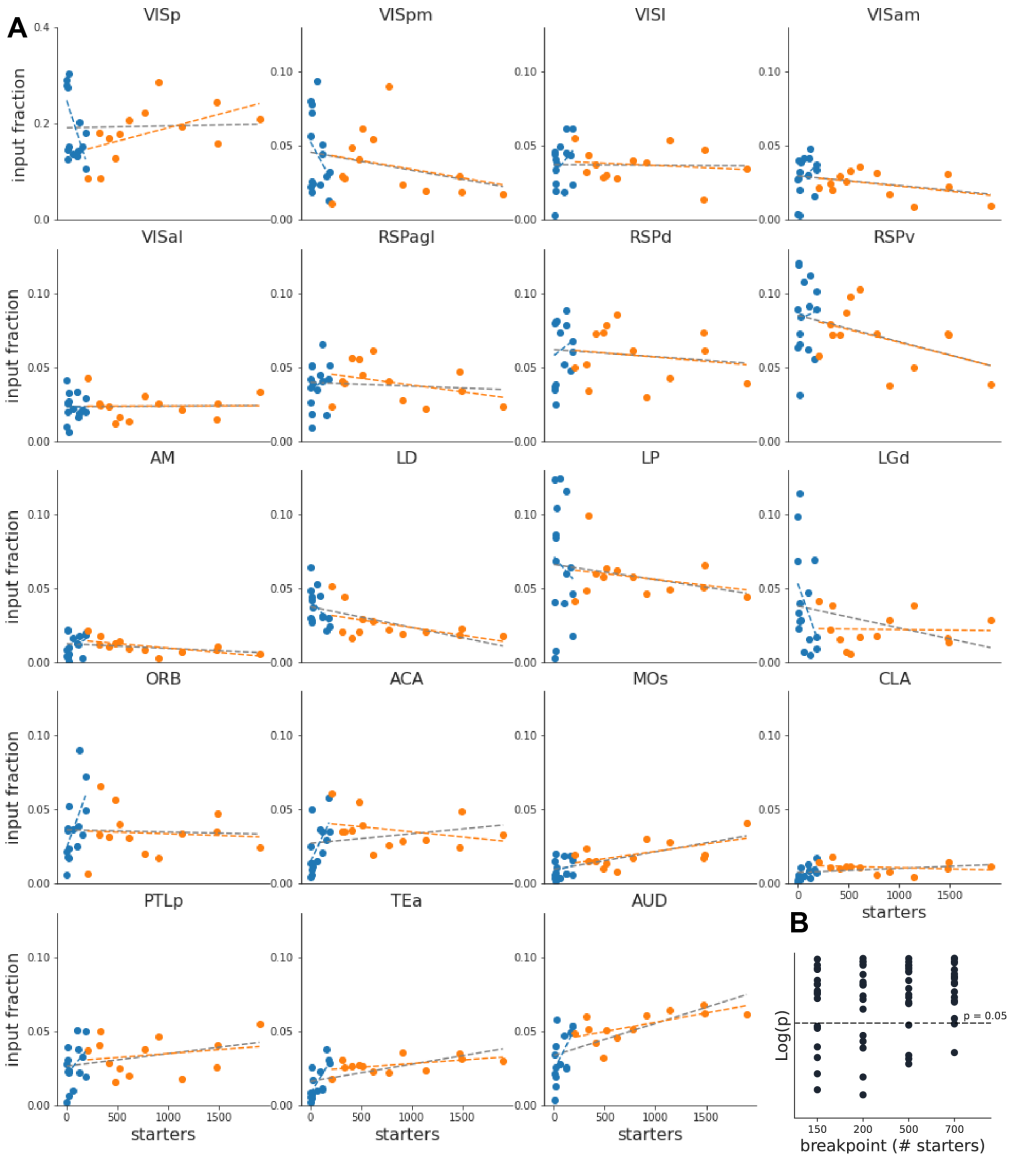

Figure S 12: **Relationship between area input maps and n_s for individual brain areas.** (A) Input fraction vs n_s. Dashed lines represent linear fit through all data (grey), for $n_s < 200$ (blue) or > 200 (orange). (B) p-value for Chow-test for varying break point values (x-axis), for individual brain areas.

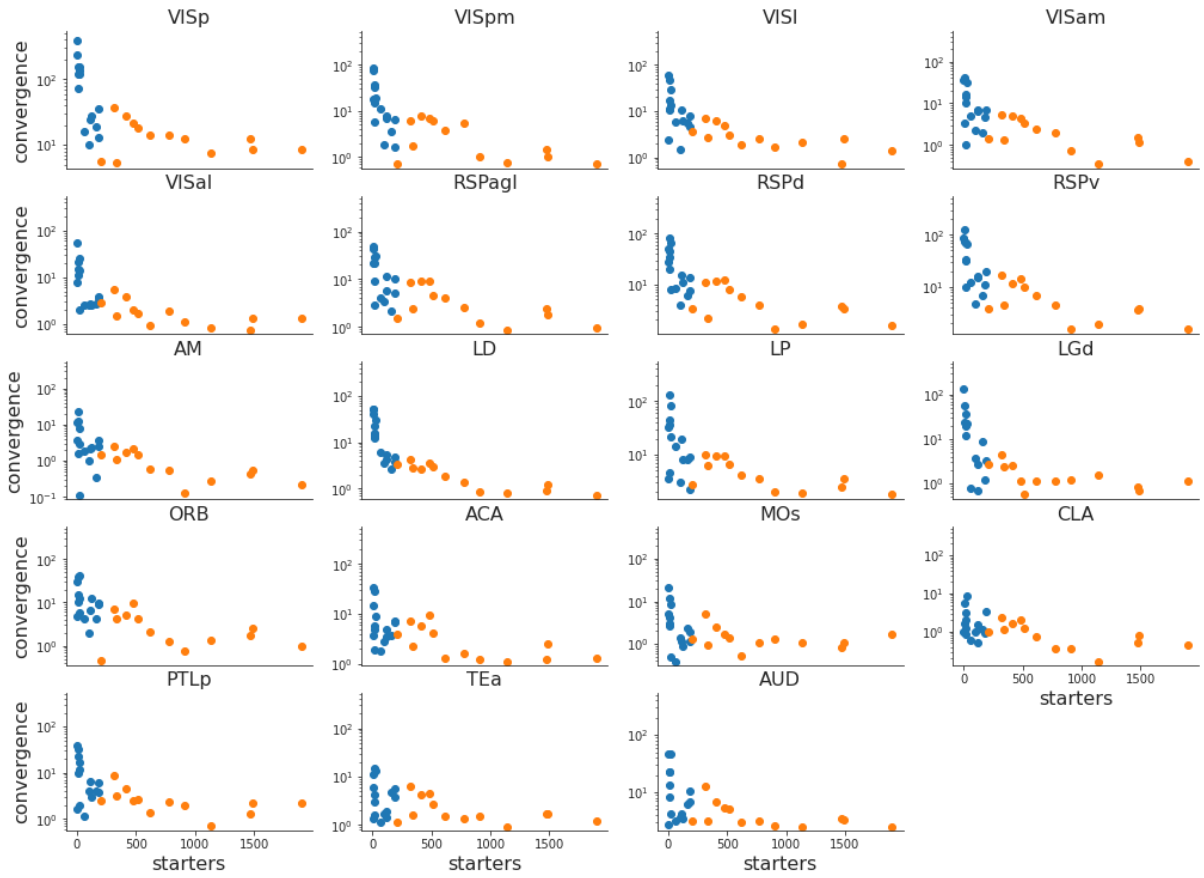

Figure S 13: **Relationship between area convergence index and n_s for individual brain areas.** Convergence index vs n_s, for $n_s < 200$ (blue) or > 200 (orange).

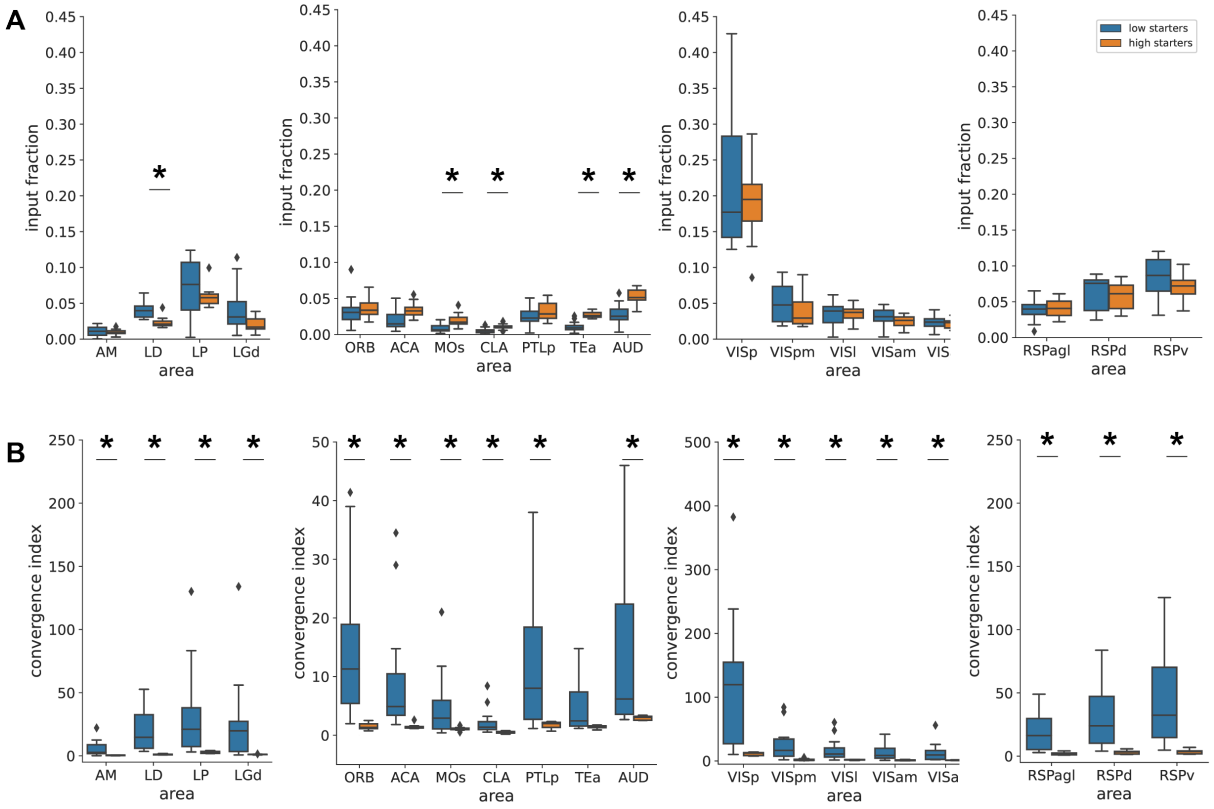

Figure S 14: **Input maps for low or high starter cell number.** (A) Area input fractions averaged across the low starter range (<125 starters, n = 10, blue) or across the high starter range (>600 starters, n = 10, orange). Statistical differences between area input fraction for low and high n_s are indicated by *. Significance was calculated using multiple t-tests corrected for multiple comparisons using the Benjamini-Hochberg method with a false discovery rate of 10%. (B) Same as A, using convergence index per area.

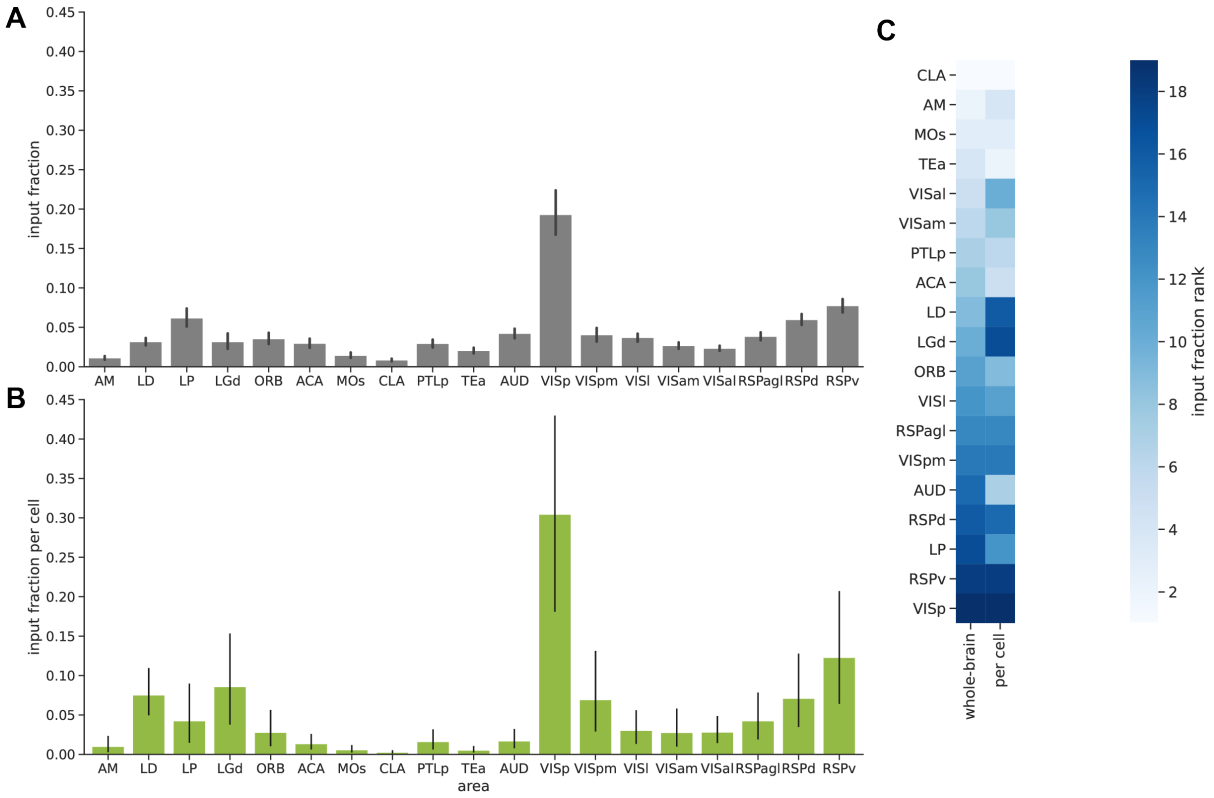

Figure S 15: **Area input fraction vs input fraction per cell for input areas.** (A) Area input fraction calculated over the full range of starter cells (error bars are s.d.) or (B) calculated from the y-intercept of $\log(n_i)$ vs $\log(n_s)$ relationship converted to linear scale (error bars are 95% confidence intervals from residuals bootstrap). (C) Areas ranks obtained via both methods are showed as a heatmap (lowest rank correspond to smallest fraction, lighter colors).

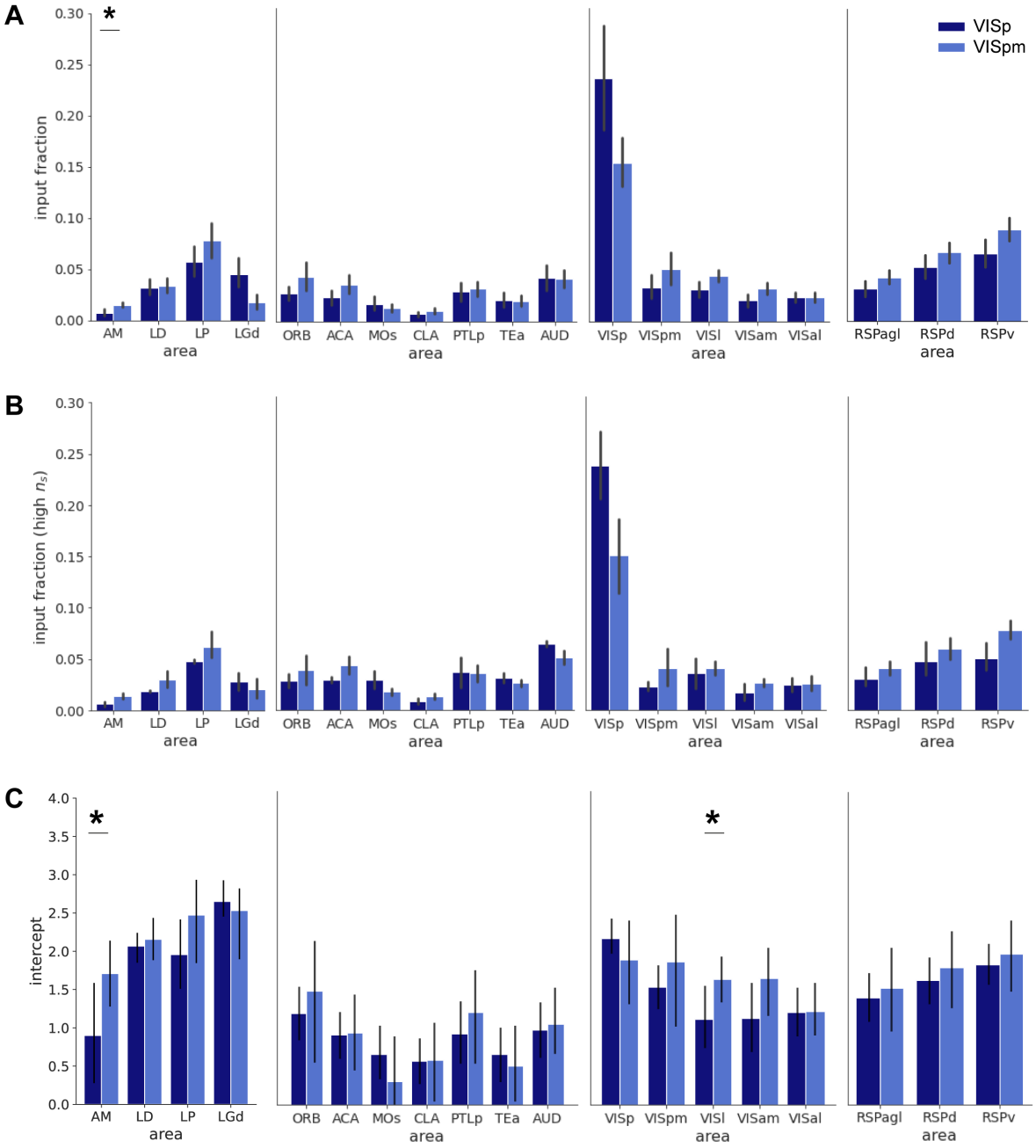

Figure S 16: **Using area input fraction or y-intercept to compare experimental parameters.** (A) Area input fraction calculated over the full range of starter cells, for experiments with target area in VISp (dark blue) or VISpm (light blue). Asterisks indicate significant difference. Significance is calculated using multiple t-tests and is corrected for multiple comparisons using the Benjamini-Hochberg method with a false discovery rate of 10%. (B) Same as A, but for n_s >200. (C) Y-intercept of log-transformed n_i vs n_s relationship. Significance is assessed by subtracting bootstrapped values of the y-intercepts between target areas. If the resulting distribution does not contain 0, the intercepts are considered significantly different. NB: areas VISp and VISpm act either as local or distal input areas, depending on the starter cells' location.

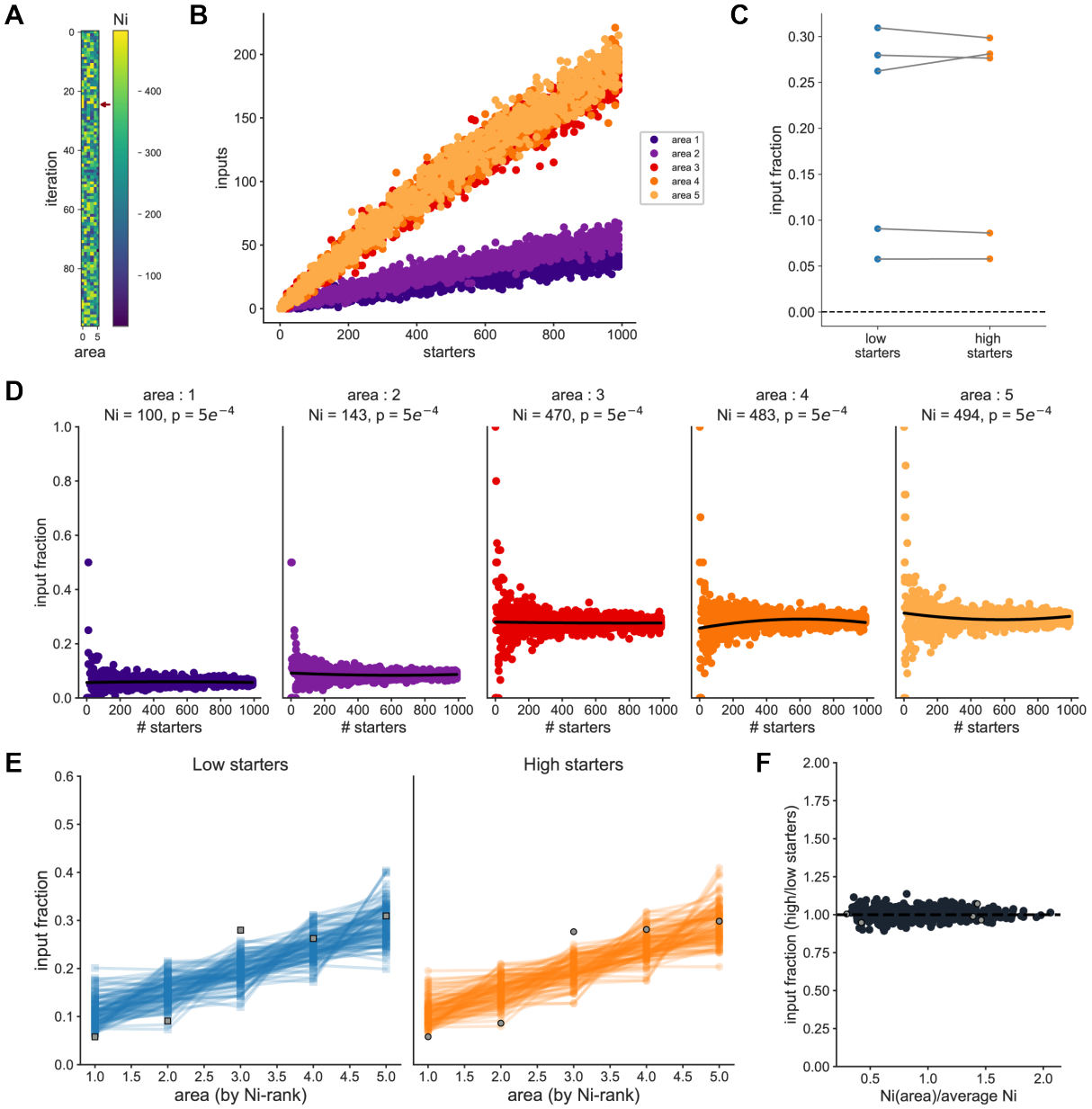

Figure S 17: **Varying relative size of input pools has no effect on area input fraction vs starter relationship.** Simulations performed using the probabilistic model with 5 input areas (100 iterations). For each iteration, the connection probability for each input area was $p = 5 * 10^{-4}$ and the size of the number of input cells N_i per area was randomly drawn between 100 and 500. (A-F), as in Figure 5.

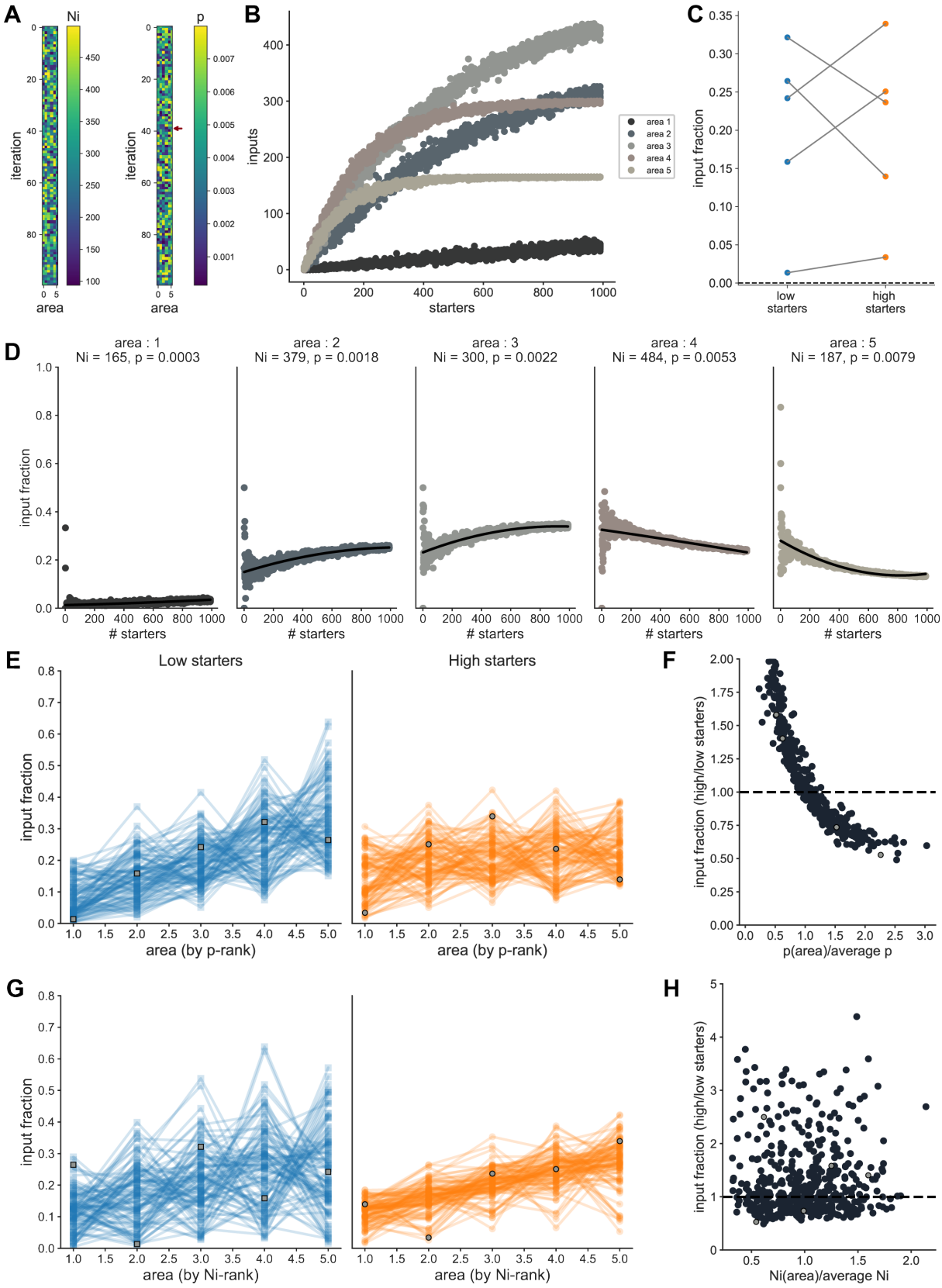

Figure S 18: **Effect of varying relative size of input pools and connection probability on area input fraction vs starter relationship.** Simulations performed using the probabilistic model with 5 input areas (100 iterations). For each simulation, the connection probability p for each input area was randomly drawn between $1 * 10^{-4}$ and $8 * 10^{-3}$ and the size of the number of input cells N_i per area was randomly drawn between 100 and 500. (A-F), as in Figure 5, (G-H), same as (E-F) but to compare the effect of relative N_i.

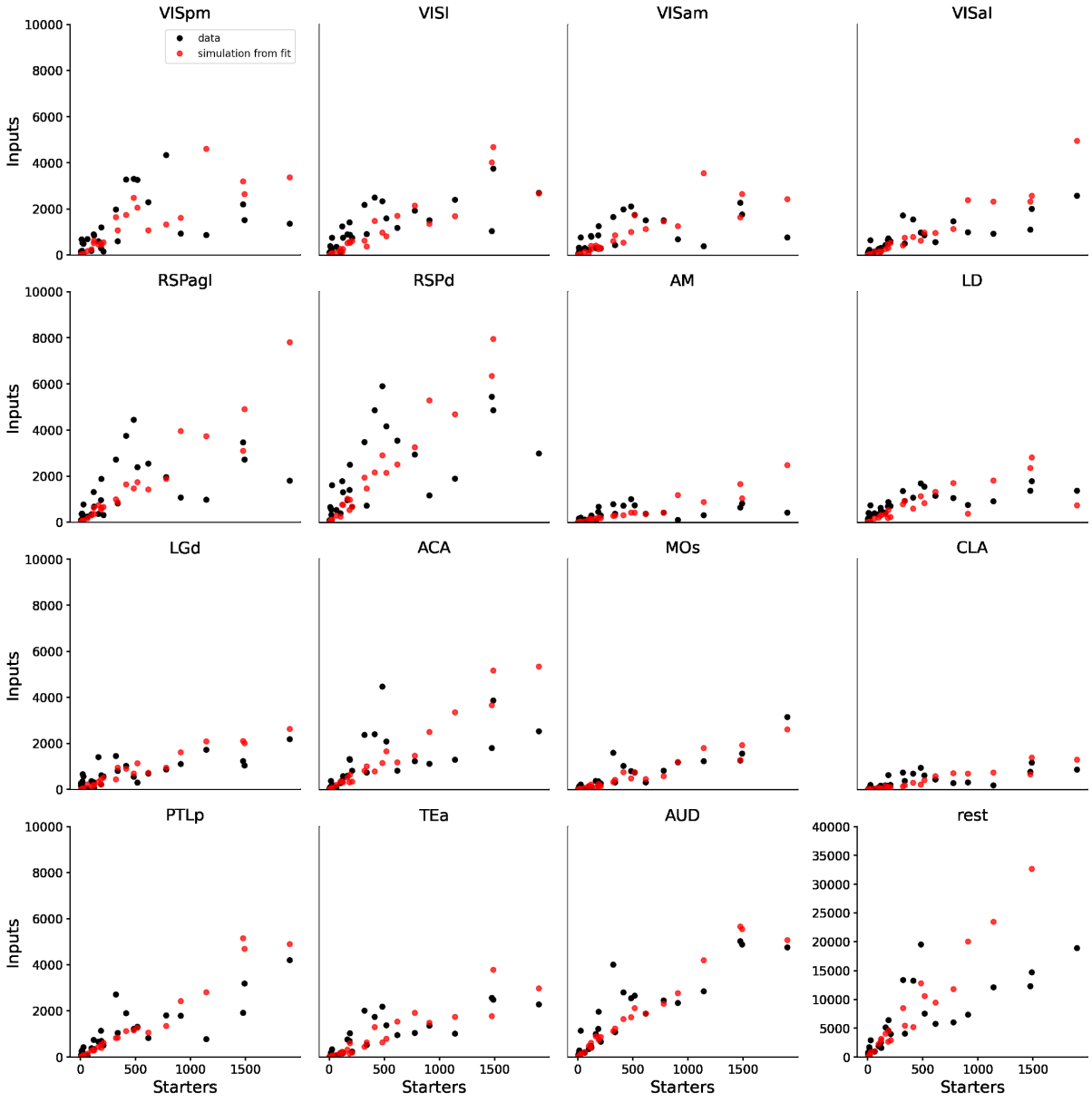

Figure S 19: **Simulation of input vs starters relationships using N_i and p obtained from fit of experimental dataset.** Input vs starters relationships for the data (black) or simulations with parameters obtained from the model fit of the data (red), for one iteration of the fit, for all areas not shown in Figure 6.

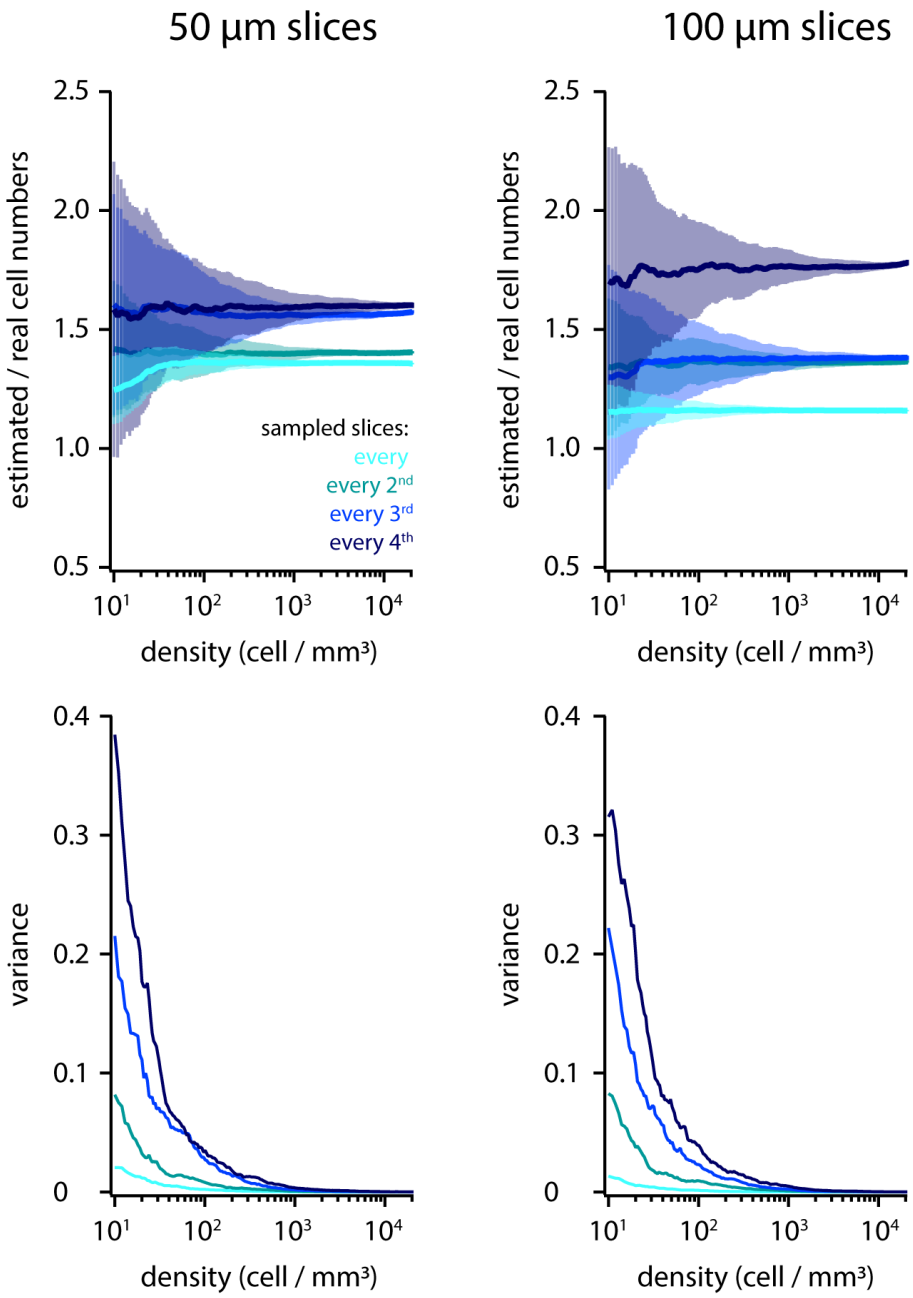

Figure S 20: **Simulation of counting cells in physically sliced tissue.** Top: the ratio between cell numbers estimated by counting in sliced tissue and the number of cells in the volume plotted versus cell density. Colours indicate slice sampling. Simulation data for two slice thicknesses, 50 and 100 μm, are shown. Bottom: variance of cell counts versus cell density for different slice sampling values and slice thickness.

References

[1] Marshel, J., Mori, T., Nielsen, K. & Callaway, E. Targeting Single Neuronal Networks for Gene Expression and Cell Labeling In Vivo. *Neuron.* **67**, 562-574 (2010,8), https://linkinghub.elsevier.com/retrieve/pii/S089662731000588X

[2] Rancz, E., Franks, K., Schwarz, M., Pichler, B., Schaefer, A. & Margrie, T. Transfection via whole-cell recording in vivo: bridging single-cell physiology, genetics and connectomics. *Nature Neuroscience.* **14**, 527-532 (2011,4), http://www.nature.com/articles/nn.2765

[3] Vélez-Fort, M., Rousseau, C., Niedworok, C., Wickersham, I., Rancz, E., Brown, A., Strom, M. & Margrie, T. The Stimulus Selectivity and Connectivity of Layer Six Principal Cells Reveals Cortical Microcircuits Underlying Visual Processing. *Neuron.* **83**, 1431-1443 (2014,9), https://linkinghub.elsevier.com/retrieve/pii/S089662731400676X

[4] Wertz, A., Trenholm, S., Yonehara, K., Hillier, D., Raics, Z., Leinweber, M., Szalay, G., Ghanem, A., Keller, G., Rózsa, B., Conzelmann, K. & Roska, B. Single-cell–initiated monosynaptic tracing reveals layer-specific cortical network modules. *Science.* **349**, 70-74 (2015,7), https://www.sciencemag.org/lookup/doi/10.1126/science.aab1687

[5] Wickersham, I., Lyon, D., Barnard, R., Mori, T., Finke, S., Conzelmann, K., Young, J. & Callaway, E. Monosynaptic Restriction of Transsynaptic Tracing from Single, Genetically Targeted Neurons. *Neuron.* **53**, 639-647 (2007,3), https://linkinghub.elsevier.com/retrieve/pii/S0896627307000785

[6] Reardon, T., Murray, A., Turi, G., Wirblich, C., Croce, K., Schnell, M., Jessell, T. & Losonczy, A. Rabies Virus CVS-N2c dG Strain Enhances Retrograde Synaptic Transfer and Neuronal Viability. *Neuron.* **89**, 711-724 (2016,2), https://linkinghub.elsevier.com/retrieve/pii/S0896627316000052

[7] Wall, N., Wickersham, I., Cetin, A., De La Parra, M. & Callaway, E. Monosynaptic circuit tracing in vivo through Cre-dependent targeting and complementation of modified rabies virus. *Proceedings Of The National Academy Of Sciences.* **107**, 21848-21853 (2010,12), http://www.pnas.org/cgi/doi/10.1073/pnas.1011756107

[8] Wall, N., Neumann, P., Beier, K., Mokhtari, A., Luo, L. & Malenka, R. Complementary Genetic Targeting and Monosynaptic Input Mapping Reveal Recruitment and Refinement of Distributed Corticostriatal Ensembles by Cocaine. *Neuron.* **104**, 916-930.e5 (2019,12), https://linkinghub.elsevier.com/retrieve/pii/S0896627319309274

[9] Schwarz, L., Miyamichi, K., Gao, X., Beier, K., Weissbourd, B., DeLoach, K., Ren, J., Ibanes, S., Malenka, R., Kremer, E. & Luo, L. Viral-genetic tracing of the input–output organization of a central noradrenaline circuit. *Nature.* **524**, 88-92 (2015,8), http://www.nature.com/articles/nature14600

[10] Watabe-Uchida, M., Zhu, L., Ogawa, S., Vamanrao, A. & Uchida, N. Whole-Brain Mapping of Direct Inputs to Midbrain Dopamine Neurons. *Neuron.* **74**, 858-873 (2012,6), https://linkinghub.elsevier.com/retrieve/pii/S0896627312002814

[11] Ogawa, S., Cohen, J., Hwang, D., Uchida, N. & Watabe-Uchida, M. Organization of Monosynaptic Inputs to the Serotonin and Dopamine

Neuromodulatory Systems. *Cell Reports*. **8**, 1105-1118 (2014,8), https://linkinghub.elsevier.com/retrieve/pii/S2211124714005269

[12] Faget, L., Osakada, F., Duan, J., Ressler, R., Johnson, A., Proudfoot, J., Yoo, J., Callaway, E. & Hnasko, T. Afferent Inputs to Neurotransmitter-Defined Cell Types in the Ventral Tegmental Area. *Cell Reports*. **15**, 2796-2808 (2016,6), https://linkinghub.elsevier.com/retrieve/pii/S2211124716306556

[13] Pouchelon, G., Dwivedi, D., Bollmann, Y., Agba, C., Xu, Q., Mirow, A., Kim, S., Qiu, Y., Sevier, E., Ritola, K., Cossart, R. & Fishell, G. The organization and development of cortical interneuron presynaptic circuits are area specific. *Cell Reports*. **37**, 109993 (2021,11), https://linkinghub.elsevier.com/retrieve/pii/S2211124721014728

[14] Sun, Q., Li, X., Ren, M., Zhao, M., Zhong, Q., Ren, Y., Luo, P., Ni, H., Zhang, X., Zhang, C., Yuan, J., Li, A., Luo, M., Gong, H. & Luo, Q. A whole-brain map of long-range inputs to GABAergic interneurons in the mouse medial prefrontal cortex. *Nature Neuroscience*. **22**, 1357-1370 (2019,8), http://www.nature.com/articles/s41593-019-0429-9

[15] Wee, R. & MacAskill, A. Biased Connectivity of Brain-wide Inputs to Ventral Subiculum Output Neurons. *Cell Reports*. **30**, 3644-3654.e6 (2020,3), https://linkinghub.elsevier.com/retrieve/pii/S2211124720302679

[16] Niedworok, C., Brown, A., Jorge Cardoso, M., Osten, P., Ourselin, S., Modat, M. & Margrie, T. aMAP is a validated pipeline for registration and segmentation of high-resolution mouse brain data. *Nature Communications*. **7**, 11879 (2016,9), http://www.nature.com/articles/ncomms11879

[17] Tyson, A., Vélez-Fort, M., Rousseau, C., Cossell, L., Tsitoura, C., Lenzi, S., Obenhaus, H., Claudi, F., Branco, T. & Margrie, T. Accurate determination of marker location within whole-brain microscopy images. *Scientific Reports*. **12**, 867 (2022,12)

[18] Hafner, G., Witte, M., Guy, J., Subhashini, N., Fenno, L., Ramakrishnan, C., Kim, Y., Deisseroth, K., Callaway, E., Oberhuber, M., Conzelmann, K. & Staiger, J. Mapping Brain-Wide Afferent Inputs of Parvalbumin-Expressing GABAergic Neurons in Barrel Cortex Reveals Local and Long-Range Circuit Motifs. *Cell Reports*. **28**, 3450-3461.e8 (2019,9), https://linkinghub.elsevier.com/retrieve/pii/S2211124719311192

[19] Beier, K., Gao, X., Xie, S., DeLoach, K., Malenka, R. & Luo, L. Topological Organization of Ventral Tegmental Area Connectivity Revealed by Viral-Genetic Dissection of Input-Output Relations. *Cell Reports*. **26**, 159-167.e6 (2019,1), https://linkinghub.elsevier.com/retrieve/pii/S2211124718319703

[20] Wall, N., De La Parra, M., Sorokin, J., Taniguchi, H., Huang, Z. & Callaway, E. Brain-Wide Maps of Synaptic Input to Cortical Interneurons. *The Journal Of Neuroscience: The Official Journal Of The Society For Neuroscience*. **36**, 4000-4009 (2016,4)

[21] Graham, K., Spruston, N. & Bloss, E. Hippocampal and thalamic afferents form distinct synaptic microcircuits in the mouse infralimbic frontal cortex. *Cell Reports*. **37**, 109837 (2021,10), https://linkinghub.elsevier.com/retrieve/pii/S2211124721013012

[22] Brown, A., Cossell, L., Strom, M., Tyson, A., Vélez-Fort, M. & Margrie, T. Analysis of segmentation ontology reveals the similarities and differences in connectivity onto L2/3 neurons in mouse V1. *Scientific Reports*. **11**, 4983 (2021,12)

[23] Yetman, M., Washburn, E., Hyun, J., Osakada, F., Hayano, Y., Zeng, H., Callaway, E., Kwon, H. & Taniguchi, H. Intersectional monosynaptic tracing for dissecting subtype-specific organization of GABAergic interneuron inputs. *Nature Neuroscience*. **22**, 492-502 (2019,3)

[24] Do, J., Xu, M., Lee, S., Chang, W., Zhang, S., Chung, S., Yung, T., Fan, J., Miyamichi, K., Luo, L. & Dan, Y. Cell type-specific long-range connections of basal forebrain circuit. *ELife*. **5** (2016,9)

[25] Kim, E., Juavinett, A., Kyubwa, E., Jacobs, M. & Callaway, E. Three Types of Cortical Layer 5 Neurons That Differ in Brain-wide Connectivity and Function. *Neuron*. **88**, 1253-1267 (2015,12), https://linkinghub.elsevier.com/retrieve/pii/S0896627315009812

[26] Sun, Y., Nguyen, A., Nguyen, J., Le, L., Saur, D., Choi, J., Callaway, E. & Xu, X. Cell-type-specific circuit connectivity of hippocampal CA1 revealed through Cre-dependent rabies tracing. *Cell Reports*. **7**, 269-280 (2014,4)

[27] Wang, Q., Ding, S., Li, Y., Royall, J., Feng, D., Lesnar, P., Graddis, N., Naeemi, M., Facer, B., Ho, A., Dolbeare, T., Blanchard, B., Dee, N., Wakeman, W., Hirokawa, K., Szafer, A., Sunkin, S., Oh, S., Bernard, A., Phillips, J., Hawrylycz, M., Koch, C., Zeng, H., Harris, J. & Ng, L. The Allen Mouse Brain Common Coordinate Framework: A 3D Reference Atlas. *Cell*. **181**, 936-953.e20 (2020,5), https://linkinghub.elsevier.com/retrieve/pii/S0092867420304025

[28] Tyson, A., Rousseau, C., Niedworok, C., Keshavarzi, S., Tsitoura, C., Cossell, L., Strom, M. & Margrie, T. A deep learning algorithm for 3D cell detection in whole mouse brain image datasets. *PLOS Computational Biology*. **17**, e1009074 (2021,5)

[29] Symonds, M. & Moussalli, A. A brief guide to model selection, multimodel inference and model averaging in behavioural ecology using Akaike's information criterion. *Behavioral Ecology And Sociobiology*. **65**, 13-21 (2011,1), http://link.springer.com/10.1007/s00265-010-1037-6

[30] Draper, N. & Smith, H. Applied regression analysis., 2nd edn (John Wiley and Sons: New York). (1981)

[31] Xiao, X., White, E., Hooten, M. & Durham, S. On the use of log-transformation vs. nonlinear regression for analyzing biological power laws. *Ecology*. **92**, 1887-1894 (2011,10), http://doi.wiley.com/10.1890/11-0538.1

[32] Fu, J., Yu, X., Zhu, Y., Xie, S., Tang, M., Yu, B. & Li, X. Whole-Brain Map of Long-Range Monosynaptic Inputs to Different Cell Types in the Amygdala of the Mouse. *Neuroscience Bulletin*. **36**, 1381-1394 (2020,11), http://link.springer.com/10.1007/s12264-020-00545-z

[33] Gehrlach, D., Weiand, C., Gaitanos, T., Cho, E., Klein, A., Hennrich, A., Conzelmann, K. & Gogolla, N. A whole-brain connectivity map of mouse insular cortex. *ELife*. **9** pp. e55585 (2020,9), https://elifesciences.org/articles/55585

[34] Vinograd, A., Tasaka, G., Kreines, L., Weiss, Y. & Mizrahi, A. The Pre-synaptic Landscape of Mitral/Tufted Cells of the Main Olfactory Bulb. *Frontiers In Neuroanatomy*. **13** pp. 58 (2019,6), https://www.frontiersin.org/article/10.3389/fnana.2019.00058/full

[35] BRAIN Initiative Cell Census Network (BICCN) & BRAIN Initiative Cell Census Network (BICCN) A multimodal cell census and atlas of the mammalian primary motor cortex. *Nature*. **598**, 86-102 (2021,10), https://www.nature.com/articles/s41586-021-03950-0

[36] Takatoh, J., Park, J., Lu, J., Li, S., Thompson, P., Han, B., Zhao, S., Kleinfeld, D., Friedman, B. & Wang, F. Constructing an adult orofacial premotor atlas in Allen mouse CCF. *ELife*. **10** pp. e67291 (2021,4), https://elifesciences.org/articles/67291

[37] Chow, G. Tests of Equality Between Sets of Coefficients in Two Linear Regressions. *Econometrica*. **28**, 591 (1960,7), https://www.jstor.org/stable/1910133?origin=crossref

[38] Kim, J., Grunke, S., Levites, Y., Golde, T. & Jankowsky, J. Intracerebroventricular Viral Injection of the Neonatal Mouse Brain for Persistent and Widespread Neuronal Transduction. *Journal Of Visualized Experiments.*, 51863 (2014,9), http://www.jove.com/video/51863/intracerebroventricular-viral-injection-neonatal-mouse-brain-for

[39] Belot, L., Albertini, A. & Gaudin, Y. Structural and cellular biology of rhabdovirus entry. *Advances In Virus Research*. **104** pp. 147-183 (2019), https://linkinghub.elsevier.com/retrieve/pii/S0065352719300132

[40] Beier, K., Kim, C., Hoerbelt, P., Hung, L., Heifets, B., DeLoach, K., Mosca, T., Neuner, S., Deisseroth, K., Luo, L. & Malenka, R. Rabies screen reveals GPe control of cocaine-triggered plasticity. *Nature*. **549**, 345-350 (2017,9), http://www.nature.com/articles/nature23888

[41] Geuna, S. & Herrera-Rincon, C. Update on stereology for light microscopy. *Cell And Tissue Research*. **360**, 5-12 (2015,4)

[42] Kim, E., Jacobs, M., Ito-Cole, T. & Callaway, E. Improved Monosynaptic Neural Circuit Tracing Using Engineered Rabies Virus Glycoproteins. *Cell Reports*. **15**, 692-699 (2016,4), https://linkinghub.elsevier.com/retrieve/pii/S2211124716303564

[43] Rogers, A. & Beier, K. Can transsynaptic viral strategies be used to reveal functional aspects of neural circuitry?. *Journal Of Neuroscience Methods*. **348** pp. 109005 (2021,1), https://linkinghub.elsevier.com/retrieve/pii/S0165027020304283

[44] Lin, R., Liang, J., Wang, R., Yan, T., Zhou, Y., Liu, Y., Feng, Q., Sun, F., Li, Y., Li, A., Gong, H. & Luo, M. The Raphe Dopamine System Controls the Expression of Incentive Memory. *Neuron*. **106**, 498-514.e8 (2020,5), https://linkinghub.elsevier.com/retrieve/pii/S0896627320301082

[45] Iascone, D., Li, Y., Sümbül, U., Doron, M., Chen, H., Andreu, V., Goudy, F., Blockus, H., Abbott, L., Segev, I., Peng, H. & Polleux, F. Whole-Neuron Synaptic Mapping Reveals Spatially Precise Excitatory/Inhibitory Balance Limiting Dendritic and Somatic Spiking. *Neuron*. **106**, 566-578.e8 (2020,5), https://linkinghub.elsevier.com/retrieve/pii/S0896627320301380

[46] Galloni, A., Ye, Z. & Rancz, E. Dendritic Domain-Specific Sampling of Long-Range Axons Shapes Feedforward and Feedback Connectivity of L5 Neurons. *The Journal Of Neuroscience*. **42**, 3394-3405 (2022,4)

[47] Han, Y., Kebschull, J., Campbell, R., Cowan, D., Imhof, F., Zador, A. & Mrsic-Flogel, T. The logic of single-cell projections from visual cortex. *Nature*. **556**, 51-56 (2018,4), http://www.nature.com/articles/nature26159

[48] Ragan, T., Kadiri, L., Venkataraju, K., Bahlmann, K., Sutin, J., Taranda, J., Arganda-Carreras, I., Kim, Y., Seung, H. & Osten, P. Serial two-photon tomography for automated ex vivo mouse brain imaging. *Nature Methods*. **9**, 255-258 (2012,3), http://www.nature.com/articles/nmeth.1854

[49] Burnham, K. & Anderson, D. Model Selection and Multimodel Inference. (Springer New York,2004), http://link.springer.com/10.1007/b97636

[50] Herculano-Houzel, S., Mota, B. & Lent, R. Cellular scaling rules for rodent brains. *Proceedings Of The National Academy Of Sciences*. **103**, 12138-12143 (2006,8), http://www.pnas.org/cgi/doi/10.1073/pnas.0604911103

[51] Keller, D., Erö, C. & Markram, H. Cell Densities in the Mouse Brain: A Systematic Review. *Frontiers In Neuroanatomy*. **12** pp. 83 (2018,10), https://www.frontiersin.org/article/10.3389/fnana.2018.00083/full